Multiscale projection-based embedded discrete fracture modeling approach for CO_2 storage in deep saline aquifers

Zhao, Mengjie; Haagenson, Ryan; Gerritsma, Marc; Hajibeygi, Hadi

DOI
10.1016/j.advwatres.2025.105200

Publication date
2026

Document Version
Final published version

Published in
Advances in Water Resources

Advances in Water Resources 207 (2026) 105200

Contents lists available at ScienceDirect

Advances in Water Resources

journal homepage: www.elsevier.com/locate/advwatres

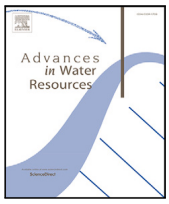

Multiscale projection-based embedded discrete fracture modeling approach for CO_2 storage in deep saline aquifers

Mengjie Zhao [a,*], Ryan Haagenson [b], Marc Gerritsma [a], Hadi Hajibeygi [c]

[a] Faculty of Aerospace Engineering, Department of Flow Physics and Technology, Delft University of Technology, Kluyverweg 2, 2629 HS, Delft, The Netherlands
[b] Faculty of Electrical Engineering, Mathematics and Computer Science, Department of Applied Mathematics, Delft University of Technology, Mekelweg 4, 2628 CD, Delft, The Netherlands
[c] Faculty of Civil Engineering and Geosciences, Department of Geoscience and Engineering, Delft University of Technology, Stevinweg 1, 2628 CV, Delft, The Netherlands

ARTICLE INFO

Keywords:
CO_2 storage
Multiscale multilevel method
Embedded discrete fracture model
Numerical simulation

ABSTRACT

This study introduces a multiscale simulation framework, termed Projection-based Embedded Discrete Fracture Modeling with Algebraic Dynamic Multilevel method (pEDFM-ADM), which integrates an embedded discrete fracture network representation with a fully algebraic, front-tracking-based mesh adaptation strategy. Incorporating a fully implicit scheme, compositional thermodynamics, and algebraic multilevel operators, the framework captures essential subsurface processes such as buoyancy-driven migration, convective dissolution, phase partitioning, and fracture-matrix interactions under geologically realistic conditions. The method constructs a hierarchy of multilevel grids and localized multiscale basis functions that introduce fine-scale heterogeneities at each coarse level. Adaptive mesh refinement and coarsening are driven by local variations in CO_2 mass fraction and executed through algebraic prolongation and restriction operators, enabling efficient projection between grid levels. The framework is systematically evaluated across a sequence of test cases with increasing complexity, including systems with low-permeability flow barriers, highly conductive fractures, striking a trade-off between computational resource and detailed simulation accuracy. Overall, the pEDFM-ADM framework provides a scalable, fully algebraic, and physically adaptive modeling tool for large-scale CO_2 storage simulations in fractured porous media, supporting predictive simulation and risk assessment for long-term carbon sequestration.

1. Introduction

Mitigating climate change requires rapid reductions in CO_2 emissions, making geological carbon capture and storage (CCS) essential as a large-scale mitigation strategy (Boot-Handford et al., 2014; Bui et al., 2018; Krevor et al., 2023; Bashir et al., 2024). Among the available geological storage options, deep saline aquifers are particularly promising due to their large storage capacities and widespread geographical distribution. These aquifers are located at depths below approximately 800 m, where CO_2 can be injected in a supercritical phase with relatively high density. Estimates suggest that the global total storage capacity of deep saline aquifers could range from hundreds to thousands of gigatons, emphasizing their critical role in global climate mitigation scenarios (Metz et al., 2005; Bachu, 2008; Alcalde et al., 2018).

Despite their potential, implementing CO_2 storage in saline aquifers presents geological and engineering challenges. A key challenge involves managing multiphase flow dynamics and trapping mechanisms during CO_2 injection and long-term storage. When CO_2 is injected into a saline reservoir, it displaces resident brine and migrates upward under buoyancy, while simultaneously dissolving into brine or becoming trapped by capillary forces in pore spaces over time (Benson and Cole, 2008; Szulczewski et al., 2012). These processes are strongly sensitive to the heterogeneities of reservoir properties, particularly the presence of natural fractures and faults. Fractures significantly impact fluid migration by creating preferential pathways or barriers, altering plume distribution and potentially influencing overall storage integrity (Rutqvist et al., 2016; Sokama-Neuyam et al., 2020). Highly conductive fractures facilitate rapid CO_2 migration, possibly leading to unintended migration beyond storage boundaries, whereas

* Corresponding author.
E-mail addresses: m.zhao-2@tudelft.nl (M. Zhao), r.haagenson@tudelft.nl (R. Haagenson), m.i.gerritsma@tudelft.nl (M. Gerritsma), h.hajibeygi@tudelft.nl (H. Hajibeygi).

https://doi.org/10.1016/j.advwatres.2025.105200
Received 22 August 2025; Received in revised form 20 December 2025; Accepted 20 December 2025
Available online 23 December 2025

low-permeability fractures act as flow barriers, compartmentalizing the reservoir and impeding the migration of CO_2 (Berkowitz, 2002; Rutqvist et al., 2010). Therefore, accurate prediction of CO_2 behavior in fractured aquifers requires advanced modeling approaches capable of integrating fine-scale fracture details with large-scale reservoir dynamics.

Among fracture modeling methods, Discrete Fracture Models (DFM) employ conforming unstructured grids to explicitly represent fractures and flow barriers at matrix interfaces (Karimi-Fard et al., 2004; Matthäi et al., 2007; Hoteit and Firoozabadi, 2008). However, generating such grids can be computationally intensive, particularly for complex fracture networks (Sahimi, 2011; Moinfar et al., 2013; Berre et al., 2019). As an alternative, Embedded Discrete Fracture Models (EDFMs) offer a more practical approach by avoiding conforming grid generation (Lee et al., 2001; Li and Lee, 2008). In EDFM, small-scale fractures entirely contained within a matrix cell are homogenized by adjusting the intrinsic permeability of the surrounding rock, while the remaining fracture networks in the network are discretized independently of the matrix grid (Hajibeygi et al., 2011; Moinfar et al., 2014). However, coupling between matrix cells and fracture cells is maintained through flux terms, even when the grid does not explicitly conform to the fracture geometry. Therefore, standard EDFM techniques struggle to accurately model fractures that are fully enclosed within a cell or have low permeability (HosseiniMehr et al., 2020). To overcome these limitations, projection-based Embedded Discrete Fracture Model (pEDFM) was developed by Ţene et al. (2017). When a fracture intersects a matrix cell, the transmissibility with a neighboring matrix cell is reduced proportionally to the projection of the fracture area onto the matrix cell face. A new connection is then created between the fracture and the neighboring matrix cell such that the permeability of the fracture determines how readily fluid flows from one matrix cell to the next. This correction ensures strict local mass conservation and reduces the error observed in original EDFM for challenging configurations involving low-permeability fractures (HosseiniMehr et al., 2022). In recent years, pEDFM has been further extended to address more complex flow mechanisms and anisotropic media, including two-phase flow simulation using hybrid TPFA-MFD formulations (Rao et al., 2024), and applications on unstructured tetrahedral grids for fully three-dimensional fractured reservoirs (Cavalcante et al., 2024). Consequently, it enables the development of a robust modeling strategy for both barrier and highly conductive fractures, while facilitating simulations of CO_2 migration and subsequent trapping processes from the injection phase to the post-migration stage (Wang et al., 2022b).

Even with such advances in modeling flow and transport in fractured reservoirs, simulating large-scale CO_2 storage remains computationally demanding, primarily due to the large spatial scales and multiscale nature of the problem. In this context, the finite volume method (FVM) is frequently employed for its efficiency and local conservation properties, making it well suited for large-scale reservoir modeling (Wang et al., 2022a,b). However, the high-resolution grids required to accurately capture flow physics and geological heterogeneity often make classical numerical solvers computational prohibitive (Praditia et al., 2018). Grids at the Darcy scale (on the order of centimeters) can generate extremely large linear systems, making conventional methods impractical for field-scale applications. Consequently, there is a demand for advanced numerical techniques that can preserve fine-scale details while ensuring computationally efficiency.

One class of solutions involves multiscale methods, such as the multiscale finite element (MsFE) (Hou and Wu, 1997; Efendiev et al., 2015) and multiscale finite volume (MsFV) approaches (Jenny et al., 2003; Lee et al., 2008; Ţene et al., 2016). These methods construct coarse-scale pressure systems that preserve critical fine-scale information through local basis functions. Algebraic restriction and prolongation operators then map the coarse-scale solution back to the original high-resolution grid, allowing an approximate solution that captures essential flow details without globally refining the entire domain (Hajibeygi et al., 2008). Building on these concepts, the Algebraic Dynamic Multilevel (ADM) method was introduced to handle fully implicit (FIM) systems on dynamically updated multilevel grids (Cusini et al., 2016, 2018). ADM addresses the coexistence of multiscale and multilevel behaviors in pressure (elliptic or parabolic) and transport (hyperbolic) unknowns by adaptively refining or coarsening the mesh at each time step based on a front-tracking criterion. This ensures that fine-scale resolution is applied only where significant gradients and physical interactions occur. Mass conservation is enforced at all levels by carefully designed finite-volume restriction operators, while pressure and transport variables are interpolated using multiscale and constant basis functions, respectively (HosseiniMehr et al., 2018).

Previously, the pEDFM and ADM methods have been applied separately to CO_2 flow and transport problems, but not within a unified modeling workflow. In this study, we develop an integrated pEDFM-ADM modeling framework specifically designed for CO_2 storage in fractured deep saline aquifers. The fractures are explicitly represented by pEDFM, allowing the study of the impact of fractures with varying permeability contrasts. ADM complements this by dynamically adjusting computational resolution, significantly enhancing efficiency while maintaining the impact of fine-scale heterogeneity on flow and transport. This integrated approach captures critical fracture-induced flow processes and large-scale reservoir dynamics, improving our predictive capability for CO_2 plume behavior and storage effectiveness. Similar to the fine-scale system, the ADM dynamic grid is constructed independently for the matrix and fractures based on a front-tracking criterion that balances computational cost with accuracy. Mapping solutions across different grid resolutions is performed using sequences of restriction and prolongation operators.

The rest of the paper is organized as follows. Section 2 outlines the governing equations for flow and transport in fractured media, as well as the discretization and simulation approach for the fine-scale, pEDFM model. Section 3 details the application of ADM to the fine-scale, pEDFM model described in Section 2. Section 4 presents numerical results demonstrating the effectiveness of the proposed approach, and Section 5 concludes the study.

2. Fine-scale model and solution strategy

Flow and transport in porous media are governed by the conservation of mass, which applies to each component across multiple coexisting phases. The representation of fluid properties relies on appropriate thermodynamic constitutive relationships that describe phase behavior under reservoir conditions. To establish a reference for subsequent multiscale development, the fine-scale model considered in this work is based on pEDFM, which resolves fracture-matrix flow interactions.

2.1. Governing equations

In geological formations, CO_2 migration is strongly affected by fracture-matrix interactions. To capture this behavior, the mass conservation equations for the CO_2-brine system in porous media with discrete embedded fractures, are formulated as:

$$\frac{\partial}{\partial t}\left(\phi^m \sum_{\alpha=1}^{n_{\mathrm{ph}}} x_{c,\alpha}\rho_\alpha S_\alpha\right) + \nabla\cdot\left(\sum_{\alpha=1}^{n_{\mathrm{ph}}} x_{c,\alpha}\rho_\alpha \mathbf{u}_\alpha\right) - \sum_{\alpha=1}^{n_{\mathrm{ph}}} x_{c,\alpha} q_\alpha - \sum_{\alpha=1}^{n_{\mathrm{ph}}} x_{c,\alpha} Q_\alpha^{mf} = 0,$$
$$\forall c \in \{1,\ldots,n_c\}, \tag{2.1}$$

for the rock matrix m and,

$$\frac{\partial}{\partial t}\left(\phi^f \sum_{\alpha=1}^{n_{\mathrm{ph}}} x_{c,\alpha}\rho_\alpha S_\alpha\right) + \nabla\cdot\left(\sum_{\alpha=1}^{n_{\mathrm{ph}}} x_{c,\alpha}\rho_\alpha \mathbf{u}_\alpha\right) - \sum_{\alpha=1}^{n_{\mathrm{ph}}} x_{c,\alpha} Q_\alpha^{fm}$$

$$-\sum_{\alpha=1}^{n_{\text{ph}}} x_{c,\alpha} Q_\alpha^{ff} = 0,$$

$$\forall c \in \{1, \ldots, n_c\}, \tag{2.2}$$

for the lower-dimensional fracture f. Here, ϕ denotes porosity, ρ_α, S_α, and q_α represent the density, saturation, and source/sink terms of the phase α (wetting or non-wetting), respectively. The subscripts $\alpha \in \{w, n\}$ denote the wetting (brine-rich) and non-wetting (CO_2-rich) phases, respectively. The index c identifies the components (CO_2 and H_2O), while $x_{c,\alpha}$ is the mass fraction of component c in phase α. The terms Q_α^{mf} and Q_α^{fm} are the phase mass flux exchanges between the rock matrix and the fractures, and Q_α^{ff} represents the phase influx between intersecting fractures. Note that the mass conservation law enforces the relations: $\iiint_V Q_\alpha^{mf} dV = -\iint_{A_i} Q_\alpha^{fm} dA$ and $\iint_{A_i} Q_\alpha^{f_i f_j} dA = -\iint_{A_j} Q_\alpha^{f_j f_i} dA$. The phase velocity $\mathbf{u}_\alpha$ is defined by Darcy's law:

$$\mathbf{u}_\alpha = -\lambda_\alpha \nabla \psi_\alpha, \tag{2.3}$$

where the phase mobility is defined as $\lambda_\alpha = \mathbf{K}\frac{k_{r,\alpha}}{\mu_\alpha}$, with μ_α as the phase viscosity, $\mathbf{K}$ as the rock permeability tensor, and $k_{r,\alpha}$ as the phase relative permeability (Abou-Kassem et al., 2013). ψ_α is the phase potential, given by:

$$\psi_\alpha = p_\alpha - \rho_\alpha g h, \tag{2.4}$$

where g is the gravitational acceleration and h is the depth. The two phase pressures p_n and p_w are interrelated by capillary pressure P_c as follows:

$$p_n - p_w = P_c. \tag{2.5}$$

Generally, the capillary pressure is a nonlinear function of the wetting-phase saturation S_w. In addition, the model assumes that the pore space is fully occupied by the phases, with CO_2 and H_2O as the only components present. This is mathematically enforced by the conditions that the sums of phase saturations and component mass fractions in each phase equal one:

$$\sum_{\alpha=w,n} S_\alpha = 1, \quad \text{and} \quad \sum_{c=\text{CO}_2,\text{H}_2\text{O}} x_{c,\alpha} = 1. \tag{2.6}$$

2.2. Thermodynamic equilibrium equations

For a binary CO_2–H_2O system, thermodynamic equilibrium is achieved when the fugacity of each component is equal in both phases (Reed, 1982):

$$f_{c,n}\left(p, x_{c,n}\right) - f_{c,w}\left(p, x_{c,w}\right) = 0, \quad \forall c \in \{\text{CO}_2, \text{H}_2\text{O}\}, \tag{2.7}$$

where $f_{c,n}$ and $f_{c,w}$ are the fugacities of component c in the non-wetting and wetting phases, respectively. This condition is often reformulated in terms of equilibrium ratios, or K-values

$$K_c = \frac{x_{c,n}}{x_{c,w}}, \tag{2.8}$$

where $x_{c,n}$ and $x_{c,w}$ are the mass fractions of component c in the vapor and aqueous phases, respectively. These K-values are functions of pressure, temperature, and salinity, and provide the basis for equilibrium-based compositional modeling (Prausnitz et al., 1998). Once K-values are evaluated, phase partitioning is determined by solving the Rachford-Rice equation for vapor fraction V (Michelsen and Mollerup, 2004):

$$\sum_{c=1}^{n_c} \frac{z_c(K_c - 1)}{1 + V(K_c - 1)} = 0, \tag{2.9}$$

where z_c is the overall mass fraction of component c, i.e.

$$z_c = \frac{\sum_{\alpha=1}^{n_{\text{ph}}} x_{c,\alpha}\rho_\alpha S_\alpha}{\sum_{\alpha=1}^{n_{\text{ph}}} \rho_\alpha S_\alpha}. \tag{2.10}$$

Fig. 1 illustrates representative results based on the thermodynamic model from Spycher et al. (2003), showing the mutual solubilities of pure CO_2 and H_2O as functions of pressure and temperature, where x_{CO_2} denotes the CO_2 mass fraction in the aqueous phase and y_{H_2O} denotes the H_2O mass fraction in the CO_2-rich phase. This model is adopted for consistency with the reservoir parameter range considered in this study. At low pressure, CO_2 solubility in the aqueous phase is relatively low. As pressure increases, the solubility of CO_2 in water increases. However, once CO_2 enters a dense or supercritical phase, its solubility becomes relatively insensitive to further pressure changes. As for the solubility of H_2O, under low-pressure conditions where CO_2 exists in a vapor state, the mass fraction of H_2O in the CO_2-rich phase is relatively high. As pressure increases within this regime, CO_2 transitions to a denser phase, leading to a marked decline in H_2O solubility. Additionally, increasing temperature enhances H_2O volatility, resulting in higher water content in the CO_2-rich phase, while simultaneously reducing CO_2 solubility in the aqueous phase.

2.3. Fine-scale solution strategy with pEDFM

The coupled non-linear Eqs. (2.1)–(2.2) for the matrix–fracture system are discretized spatially using the two-point-flux approximation (TPFA) finite volume method, and temporally using the backward Euler scheme, resulting in a FIM system. Independent structured grids are generated for a three-dimensional (3D) aquifer and a network of two-dimensional (2D) fractures. An illustration is presented in Fig. 2 for a simple scenario with just two fractures.

The fracture-matrix coupling terms corresponding to Eqs. (2.1)–(2.2) are modeled following the approach of Li and Lee (2008) and Hajibeygi et al. (2011). For a matrix control volume i having an embedded fracture element f, the flux of component c in phase α across the matrix–fracture interface is expressed as

$$Q_{\alpha,if} = \rho_\alpha \frac{k_{r,\alpha}}{\mu_\alpha} T_{if} \Delta\psi_{\alpha,if}, \tag{2.11}$$

where the rock transmissibility between the matrix and the fracture T_{if} is defined symmetrically as

$$T_{fi} = T_{if} = CI_{if} K_{if}^H. \tag{2.12}$$

Here, K_{if}^H is the harmonic average permeability between the overlapping matrix and fracture elements. The mobility is evaluated using a phase potential upwind scheme. CI_{if} denotes the connectivity index (Hajibeygi et al., 2011), calculated as

$$CI_{if} = \frac{S_{if}}{\langle d_{if} \rangle}, \tag{2.13}$$

where $\langle d_{if} \rangle$ represents the average distance between the matrix control volume and the fracture surface. The fracture–matrix fluxes satisfy the local conservation property $F_{c,\alpha,if} = -F_{c,\alpha,fi}$. To correct for the limitations of the original EDFM when handling fractures with generic conductivity due to parallel transmissibilities, the pEDFM modifies the matrix–matrix, matrix–fracture, and fracture–fracture connectivities within overlapping regions. A continuous projection path is automatically established at the matrix–fracture interfaces, ensuring that flux exchange occurs only through the physical connection between the two domains. For each spatial direction $x_e \in \{x, y, z\}$, the corresponding projected area fraction on the interface between cell i and its neighboring cells (e.g., j or k) is given by:

$$S_{if\perp x_e} = A_{if} \times \cos(\theta), \tag{2.14}$$

where A_{if} is the area fraction of the fracture cell f overlapping with the rock matrix cell i, and θ is the angle between the fracture plane and the interface connecting the matrix grid cell i and its neighboring cell in the corresponding direction. Further details of the geometric projection and transmissibility correction procedures can be found in Şene et al. (2017).

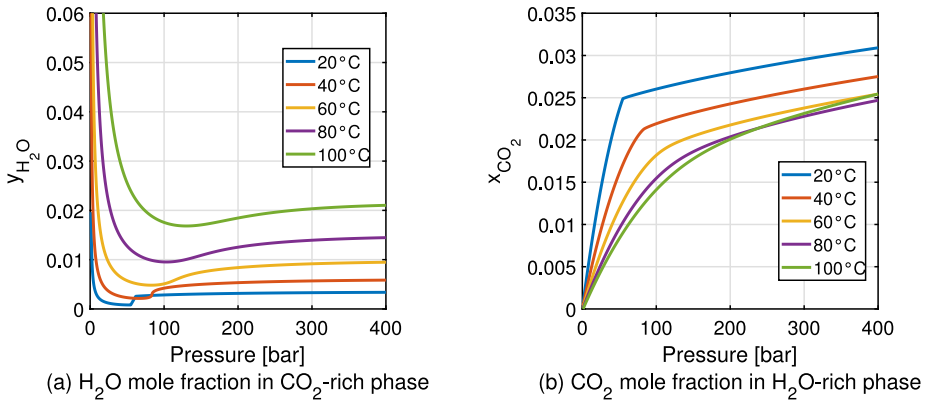

Fig. 1. Mutual solubilities of H_2O and CO_2 from 20 to 100 °C and up to a pressure of 400 bar, based on the model of Spycher et al. (2003) and adapted from (Zhao et al., 2025).

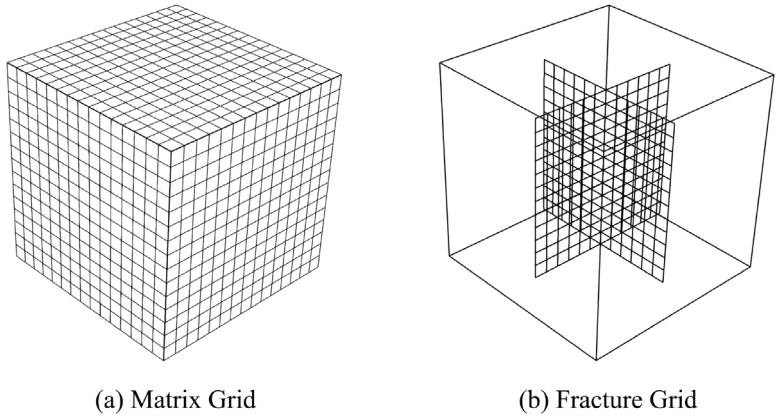

Fig. 2. The independent numerical grids: (a) 3D grid for rock matrix and (b) 2D grids for fractures.

The discrete residual form of Eq. (2.1) for component c in cell $\langle i\rangle$ within the rock matrix is written as:

$$\begin{aligned} r^m_{c,\langle i\rangle} = {} & \frac{V^m_{\langle i\rangle}\phi^m_{\langle i\rangle}}{\Delta t}\sum_{\alpha=1}^{n_{\text{ph}}}\left(x^{t+1}_{c,\alpha,\langle i\rangle}\rho^{t+1}_{\alpha,\langle i\rangle}S^{t+1}_{\alpha,\langle i\rangle} - x^{t}_{c,\alpha,\langle i\rangle}\rho^{t}_{\alpha,\langle i\rangle}S^{t}_{\alpha,\langle i\rangle}\right) \\ & + \sum_{j=1}^{N_n}\sum_{\alpha=1}^{n_{\text{ph}}} x_{c,\alpha}\rho_\alpha \mathbf{u}_\alpha\Big|^{t+1}_{\langle ij\rangle}\cdot\vec{\mathbf{n}} \\ & - \sum_{\alpha=1}^{n_{\text{ph}}} x^{t+1}_{c,\alpha} q^{m,t+1}_{\alpha,\langle i\rangle} - \sum_{f=1}^{N_f}\sum_{\alpha=1}^{n_{\text{ph}}} x^{t+1}_{c,\alpha,\langle i\rangle} Q^{if,t+1}_{\alpha,\langle i\rangle} = 0, \end{aligned} \tag{2.15}$$

while for the fracture space it is written as:

$$\begin{aligned} r^f_{c,\langle i\rangle} = {} & \frac{V^f_{\langle i\rangle}\phi^f_{\langle i\rangle}}{\Delta t}\sum_{\alpha=1}^{n_{\text{ph}}}\left(x^{t+1}_{c,\alpha,\langle i\rangle}\rho^{t+1}_{\alpha,\langle i\rangle}S^{t+1}_{\alpha,\langle i\rangle} - x^{t}_{c,\alpha,\langle i\rangle}\rho^{t}_{\alpha,\langle i\rangle}S^{t}_{\alpha,\langle i\rangle}\right) \\ & + \sum_{j=1}^{N_n}\sum_{\alpha=1}^{n_{\text{ph}}} x_{c,\alpha}\rho_\alpha \mathbf{u}_\alpha\Big|^{t+1}_{\langle ij\rangle}\cdot\vec{\mathbf{n}} \\ & - \sum_{m=1}^{N_m}\sum_{\alpha=1}^{n_{\text{ph}}} x^{t+1}_{c,\alpha,\langle i\rangle} Q^{im,t+1}_{\alpha,\langle i\rangle} - \sum_{f=1}^{N_f}\sum_{\alpha=1}^{n_{\text{ph}}} x^{t+1}_{c,\alpha,\langle i\rangle} Q^{if,t+1}_{\alpha,\langle i\rangle} = 0. \end{aligned} \tag{2.16}$$

Here, N_n denotes the number neighboring cells that surround the cell $\langle i\rangle$ in the corresponding media. N_m and N_f are the number of matrix and of fracture cells in the entire system, respectively. The overall-composition variable set is employed (Voskov and Tchelepi, 2012), in which the wetting phase pressure, p_w, and overall CO_2 mole (mass) fraction, z_{CO_2}, are used as primary variables (Wang et al., 2022b).

To solve the nonlinear system at each time-step, the Newton–Raphson method is employed, starting with a first-order Taylor series expansion of the residual equations about the current iteration ν:

$$r_c^{\nu+1} \approx r_c^{\nu} + \left.\frac{\partial r_c}{\partial p_w}\right|_{\nu}\delta p_w^{\nu+1} + \left.\frac{\partial r_c}{\partial z_{CO_2}}\right|_{\nu}\delta z_{CO_2}^{\nu+1}, \tag{2.17}$$

where ν and $\nu+1$ indicate the iteration steps. $\delta p_w^{\nu+1}$ and $\delta z_{CO_2}^{\nu+1}$ are the updates of the unknowns at iteration $\nu+1$. This procedure leads to a system of linearized equations that can be expressed in a matrix form:

$$\underbrace{\begin{bmatrix} J^{mm}_{CO_2,p_w} & J^{mf}_{CO_2,p_w} & J^{mm}_{CO_2,z_{CO_2}} & J^{mf}_{CO_2,z_{CO_2}} \\ J^{fm}_{CO_2,p_w} & J^{ff}_{CO_2,p_w} & J^{fm}_{CO_2,z_{CO_2}} & J^{ff}_{CO_2,z_{CO_2}} \\ J^{mm}_{H_2O,p_w} & J^{mf}_{H_2O,p_w} & J^{mm}_{H_2O,z_{CO_2}} & J^{mf}_{H_2O,z_{CO_2}} \\ J^{fm}_{H_2O,p_w} & J^{ff}_{H_2O,p_w} & J^{fm}_{H_2O,z_{CO_2}} & J^{ff}_{H_2O,z_{CO_2}} \end{bmatrix}^{\nu}}_{\mathbf{J}^{\nu}} \underbrace{\begin{bmatrix} \delta p^m_w \\ \delta p^f_w \\ \delta z^m_{CO_2} \\ \delta z^f_{CO_2} \end{bmatrix}^{\nu+1}}_{\delta\xi^{\nu+1}} = -\underbrace{\begin{bmatrix} r^m_{CO_2} \\ r^f_{CO_2} \\ r^m_{H_2O} \\ r^f_{H_2O} \end{bmatrix}^{\nu}}_{r^{\nu}}. \tag{2.18}$$

Here, $\mathbf{J}^{\nu}$ is the Jacobian (derivatives) matrix, $\delta\xi^{\nu+1}$ is the vector of unknown increments, and r^{ν} is the residual vector. The linearized system is solved iteratively until convergence is reached, typically indicated by sufficiently small changes in the primary variables or by achieving a low residual norm. This completes the description of the pEDFM approach used as the fine-scale model in this study. The next section introduces the application of ADM within this framework.

3. pEDFM-ADM for CO_2 storage

The pEDFM-ADM framework integrates pEDFM with the ADM method to efficiently simulate multiphase, CO_2–H_2O flow in fractured saline aquifers. In this approach, the fractured aquifer is discretized

on a Cartesian grid, with fractures embedded as lower-dimensional features using pEDFM. The ADM component introduces a dynamic multilevel hierarchy that enables efficient simulation by solving the governing equations on coarser grids and reconstructing fine-scale solutions via multiscale interpolator. This approach allows accurate resolution of key features, such as CO_2 fronts or active fractures, without globally refining the grid.

3.1. Adaptive selection of multilevel grids

At each time-step, the pEDFM-ADM framework adaptively constructs a multilevel solution grid by combining predefined sets of matrix and fracture grid cells. The grid is refined or coarsened dynamically based on the evolving physical state of the system, particularly the movement of the CO_2 concentration front, which is identified according to a user-defined threshold. For instance, the algorithm tracks the overall mass fraction z_{CO_2} and applies fine resolution in regions with steep gradients, while coarsening areas where CO_2 mass fracture evolves more smoothly. This front-tracking strategy ensures efficient use of computational resources without compromising accuracy.

For a three-dimensional aquifer, the physical domain is initially discretized into a fine-scale grid consisting of N_m cells in the rock matrix and N_{f_i} cells for each fracture i. Although this resolution captures detailed CO_2-brine interactions, solving fully implicit systems across all cells becomes computationally prohibitive for large-scale problems. To address this, pEDFM-ADM constructs a hierarchy of coarser grids, indexed by level l, where $l = 0$ corresponds to the fine-scale grid. Let N_m^l and $N_{f_i}^l$ denote the number of control volumes at level l in the matrix and in fracture i, respectively. The coarsening ratio γ^l at level l is defined as:

$$\gamma^l = \left(\gamma_m^l, \gamma_{f_1}^l, \dots, \gamma_{f_{N_f}}^l\right) = \left(\frac{N_m^l}{N_m^{l-1}}, \frac{N_{f_1}^l}{N_{f_1}^{l-1}}, \dots, \frac{N_{f_{n_{\text{frac}}}}^l}{N_{f_{n_{\text{frac}}}}^{l-1}}\right). \tag{3.1}$$

This framework allows for independent coarsening strategies in the matrix and individual fractures, offering flexibility. To maintain numerical stability, the level difference between neighboring cells is restricted to one, thereby avoiding abrupt transitions that could degrade solution quality.

The selection of the grid resolution is guided by a threshold-based criterion, specified as an input parameter. This refinement criterion compares the spatial variation of z_{CO_2} between neighboring cells. Let Ω_l^I and Ω_l^J denote two neighboring coarse grid cells at level l, and i and j indicate the indices of fine-scale cells contained in these coarse blocks. The maximum difference of the z_{CO_2} is computed as:

$$\Delta z_{I,J} = \max_{i \in \Omega_l^I,\ j \in \Omega_l^J} \left| z_i - z_j \right|. \tag{3.2}$$

If the difference $\Delta z_{I,J}$ for any pair of neighboring coarse blocks exceeds a specified threshold, the block I is refined from coarse level l to $(l-1)$.

3.2. Solution strategy

At each Newton iteration, pEDFM-ADM constructs a reduced multiscale system via algebraic operators based on Eq. (2.18), defined on a dynamic multilevel grid updated at the beginning of each time-step. In regions where a coarse grid is employed, a fine-scale solution that accounts for subgrid-scale heterogeneity can be efficiently reconstructed from the coarse-scale solution using algebraically defined restriction ($\mathbf{R}$) and prolongation ($\mathbf{P}$) operators. These operators are constructed to ensure local mass conservation in the reconstructed fine-scale fields. The underlying ADM methodology is described in detail by Cusini et al. (2016). Fig. 3 provides a schematic overview of how the pEDFM-ADM method is applied to CO_2 storage.

The fully-implicit system on the fine grid is projected to a selected coarser level l by restriction and prolongation operators:

$$\underbrace{\hat{\mathbf{R}}_l^{l-1} \cdots \hat{\mathbf{R}}_1^0 \mathbf{J}_0 \hat{\mathbf{P}}_0^1 \cdots \hat{\mathbf{P}}_{l-1}^l}_{\mathbf{J}_{\text{ADM}}} \delta\xi_l' = -\underbrace{\hat{\mathbf{R}}_l^{l-1} \cdots \hat{\mathbf{R}}_1^0 r_0}_{r_{\text{ADM}}}, \tag{3.3}$$

where $\mathbf{J}_0$ and r_0 are the Jacobian matrix and residual vector at the fine scale, respectively, and $\delta\xi_l'$ is the solution at grid level l. The restriction operators $\hat{\mathbf{R}}_l^{l-1}$ map residuals of governing equations from level $l-1$ to level l, while the prolongation operators $\hat{\mathbf{P}}_{l-1}^l$ interpolate the solution in the opposite direction. Both $\mathbf{R}$ and $\mathbf{P}$ are block-diagonal matrices:

$$\mathbf{R}_l^{l-1} = \begin{pmatrix} \left[(R_p)_l^{l-1}\right]_m & 0 & 0 & 0 \\ 0 & \left[(R_p)_l^{l-1}\right]_f & 0 & 0 \\ 0 & 0 & \left[(R_z)_l^{l-1}\right]_m & 0 \\ 0 & 0 & 0 & \left[(R_z)_l^{l-1}\right]_f \end{pmatrix}_{N_l \times N_{l-1}}, \tag{3.4}$$

and

$$\mathbf{P}_{l-1}^l = \begin{pmatrix} \left[(P_p)_{l-1}^l\right]_{mm} & \left[(P_p)_{l-1}^l\right]_{mf} & 0 & 0 \\ \left[(P_p)_{l-1}^l\right]_{fm} & \left[(P_p)_{l-1}^l\right]_{ff} & 0 & 0 \\ 0 & 0 & \left[(P_z)_{l-1}^l\right]_{mm} & 0 \\ 0 & 0 & 0 & \left[(P_z)_{l-1}^l\right]_{ff} \end{pmatrix}_{N_{l-1} \times N_l}. \tag{3.5}$$

Here, the subscript p and z denote the liquid pressure and overall CO_2 mass fraction sub-blocks, respectively. The same finite-volume restriction operator is typically applied to both variables to ensure the local mass balance, meaning $(R_p)_l^{l-1} = (R_z)_l^{l-1}$. Each entry of the restriction operator $(R_p)_l^{l-1}$ is binary:

$$(R_p)_l^{l-1}(i,j) = \begin{cases} 1 & \text{if cell } j \text{ is inside coarser cell } i, \\ 0 & \text{otherwise.} \end{cases} \tag{3.6}$$

Once the grid hierarchy is established, solving the coarser system and then prolonging the solution back to the fine grid provides an approximation to the fully resolved, fine-scale solution. This process significantly reduces computational costs compared to solving the original fine-scale system in all cells. The final step involves recovering the fine-scale solution $\delta\xi_0$ by iteratively applying all prolongation operators:

$$\delta\xi_0 \approx \delta\xi_0' = \hat{\mathbf{P}}_0^1 \dots \hat{\mathbf{P}}_{l-1}^l \delta\xi_l'. \tag{3.7}$$

Previous studies have shown that an iterative procedure is needed for highly-heterogeneous reservoirs (Hajibeygi et al., 2008). To this end, the pEDFM-ADM method integrates two iterations of a fine-scale smoother to reduce remaining errors to a desired tolerance. This smoother approximates the inverse of the original fine-scale linear operator $\mathbf{A}^\nu$, and is implemented using ILU(0) decomposition.

3.3. Fracture multilevel multiscale basis functions

In the pEDFM-ADM framework, a non-overlapping primal coarse grid is first constructed on the fine-scale computational domain for both the matrix and fracture cells. By connecting the coarse nodes, an overlapping decomposition is obtained, referred to as the dual coarse grid, as described by Cusini et al. (2016). Local basis functions are then computed for each coarse node within its dual coarse block, following the multilevel grid hierarchy. For hyperbolic variables (e.g., saturation or component mass fraction), constant interpolation is adopted as the prolongation operator, while for the elliptic pressure field, multiscale basis functions following Ţene et al. (2016) are employed to account for heterogeneity in transmissibility.

As with the typical pEDFM method, fractures are discretized as lower-dimensional entities embedded in the matrix grid. Coarse nodes

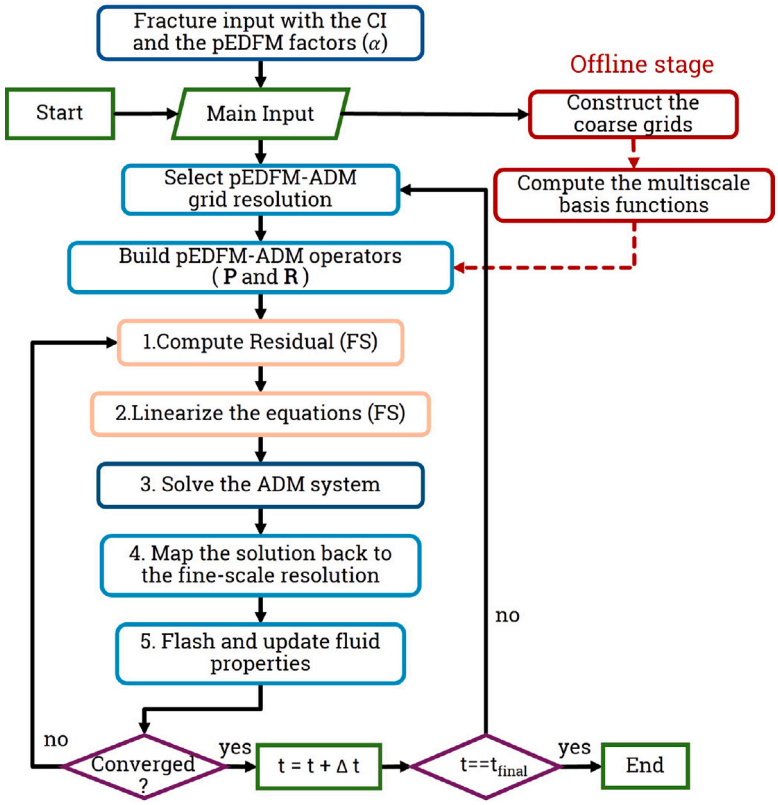

Fig. 3. Schematic description of the pEDFM-ADM strategy.

are assigned in the fracture domain similarly to the matrix, ensuring that every fracture contains its own set of coarse nodes. As a result, basis functions are constructed not only for matrix coarse nodes but also for fracture coarse nodes. The computation of fracture basis functions follows a similar procedure to that of the matrix; however, the support region of each basis function now extends across both the matrix and fracture media.

This coupling implies that matrix basis functions are influenced by the presence of nearby fractures, and meanwhile, fracture basis functions are also affected by adjacent matrix cells. The resulting basis functions are therefore termed fully coupled basis functions, as they are solved over local dual coarse domains that include both matrix and fracture cells, with all intermediate interactions preserved.

Mathematically, for each coarse node i, the local basis function Φ_i is obtained by solving the following coupled system over its local domain Ω_i, i.e.,

$$-\nabla\cdot\left(\lambda^*\,\nabla\Phi_i^{*\bullet}\right)+\sum_{j\in \mathrm{conn}_{mf}^*}\eta_j^*\,C\left(\Phi_i^{*\bullet}\right)+\sum_{j\in \mathrm{perf}_w^*}\beta_j^*\left(\Phi_i^{*\bullet}-\Phi_i^{w\bullet}\right)=0, \tag{3.8}$$

which is solved for each basis function $\Phi_i^{*\bullet}$. Here, η_j^* is the matrix–fracture coupling coefficient, and β_j^* is the well index if wells are present. The operator $C(\cdot)$ denotes the matrix–fracture coupling term. A detailed description of the basis function entries can be found in Ţene et al. (2016). The solution Φ_i is then assembled into column i of the prolongation operator P_p, which maps coarse pressures to the fine-scale solution. These multiscale basis functions enable accurate coarse-grid representation of flow in highly heterogeneous porous media with complex matrix–fracture connectivity. Fig. 4 shows a surface plot of some matrix and fracture basis functions at two different coarsening levels for a 2D homogeneous domain.

4. Numerical results

This section presents a series of numerical simulations designed to evaluate the effectiveness of the proposed framework. We begin by analyzing the influence of fractures on CO_2 sequestration performance, and then proceed to more complex scenarios to assess both the accuracy and computational efficiency of the method.

The relative permeability curves for the matrix domain are modified based on experimental data reported in Oak et al. (1990), and are modeled using the Van Genuchten formulation (Van Genuchten, 1980). Capillary pressure curves are derived from the Leverett J-function. In this study, we assume that multiphase interactions within the fractures are negligible. Consequently, the relative permeability in fractures follows linear functions (Fanchi, 2005), and both capillary pressure and hysteresis effects are neglected in the fracture domain. The primary drainage and imbibition curves for the matrix are illustrated in Fig. 5.

We assess the accuracy of the pEDFM-ADM method by comparing it with a reference fine-scale simulation that employs the pEDFM method without ADM. To quantify the solution accuracy of pEDFM-ADM method for hyperbolic variables (e.g., x_{CO_2} and z_{CO_2}), the error at each time step t is defined as Zhao et al. (2025):

$$\epsilon_x(t)=\frac{\sum_{i=1}^{N}\left|x^i_{CO_2}(t)-x^i_{CO_2,\mathrm{ref}}(t)\right|}{N}, \tag{4.1}$$

where $x_{CO_2,ref}$ is the reference fine-scale solution for the CO_2 mass fraction, and N is the total number of fine cells. For pressure, we define the normalized root-mean-square error as:

$$\epsilon_P(t)=\frac{\sqrt{\frac{1}{N}\sum_{i=1}^{N}\left(P^i_w(t)-P^i_{w,\mathrm{ref}}(t)\right)^2}}{P_{bc}}, \tag{4.2}$$

where $P_{w,ref}$ denotes the fine-scale solution of the wetting-phase pressure, and P_{bc} is a characteristic pressure scale (for instance, a boundary value). The average errors over the entire simulation period are computed to provide a global measure of solution accuracy:

$$\epsilon_x=\mathrm{mean}(\epsilon_x(t)), \tag{4.3}$$

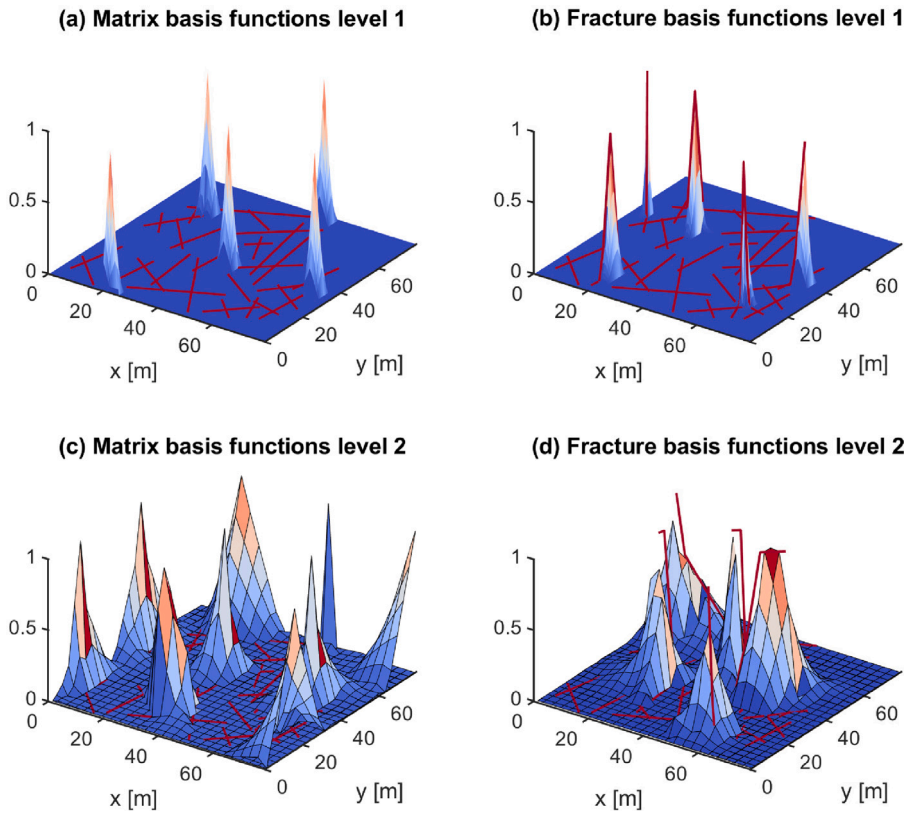

Fig. 4. Example of multilevel, fully coupled basis functions over multiple dual coarse blocks in a 2D homogeneous fractured domain. Red lines indicate the fracture network, and the basis functions capture both matrix and fracture influences. The color scale represents the magnitude of the pressure basis function.

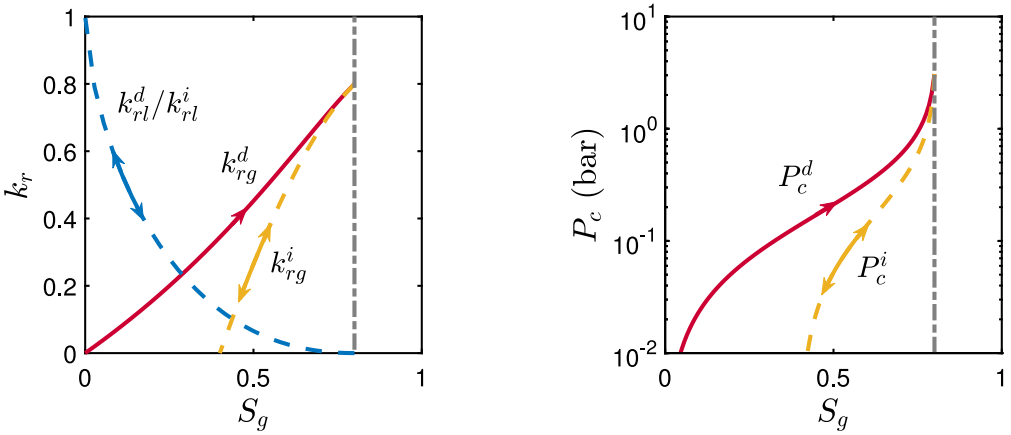

Fig. 5. Illustrations of the relative permeability and capillary pressure curves used for the matrix domain. Superscripts d and i denote drainage and imbibition, respectively. Single-headed arrows indicate irreversible processes, while double-headed arrows represent reversible ones along the corresponding curves.

$$\epsilon_P = \text{mean}(\epsilon_P(t)). \tag{4.4}$$

4.1. Test case 1: Impacts of fractures

To systematically investigate the full-cycle behavior of CO_2 storage in a deep fractured saline aquifer, we first consider a two-dimensional conceptual model representing a reservoir cross-section with a length of 200 m and a height of 50 m. The domain is discretized into a structured grid with 201 cells in the horizontal direction and 51 cells in the vertical direction. The permeability of the rock matrix is set to 8×10^{-14} m^2. A CO_2 injection well is placed on the left boundary, injecting through the bottom 10 m of the formation, while a production well penetrating the full vertical extent of the domain is located at the right boundary. The production well is designed to withdraw formation brine rather than produced CO_2, in order to mitigate pressure perturbations and facilitate CO_2 dispersal throughout the aquifer. Two inclined fractures are embedded in the domain with identical inclination angles but different spatial positions, as shown in Fig. 6.

To evaluate the impact of fracture conductivity, we vary the fracture permeability while keeping the fracture aperture constant. In each scenario, we consider two logarithmic-scale fracture-to-matrix permeability ratios, defined as $\log_{10}(k_f/k_m)$, with values of 4 and −6 representing highly conductive fractures and near-impermeable flow barriers, respectively. The physical parameters and simulation settings used in all scenarios are summarized in Table 1.

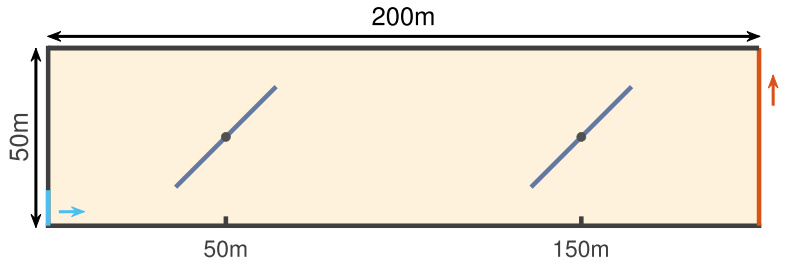

Fig. 6. Schematic of 200 × 50 m computational domain and fracture configurations used in Test Case 1. The injector is shown in light blue, the producer in red, and each fracture in dark blue.

Table 1
Physical parameters and simulation setup. (STC: standard conditions.)

Parameter	Value	Unit
Aquifer length	200	m
Aquifer height	50	m
Fracture length	40	m
Fracture aperture	5×10^{-3}	m
Fracture inclination angle	45	°
Matrix porosity	0.2	–
Matrix permeability	8×10^{-14}	m^2
Initial pressure	25	MPa
Bottom hole pressure	25	MPa
Temperature	323.15	K
Injection rate	1×10^{-4}	pore volume/day
CO_2 density at STC	1.98	kg/m^3
H_2O density at STC	998	kg/m^3
Simulation time	3.2×10^4	day
Injection time	600	day

Fig. 7 presents streamline patterns of aqueous phase under three configurations: the base case simulation without fractures, flow barrier fractures, and finally conductive fractures. In Fig. 7(b), streamlines are visibly diverted around the low-permeability fractures, most clearly near the fracture tips where stagnation zones form. Almost no streamlines pass through the fractures, confirming their role as effective flow barriers. In contrast, in Fig. 7(c), where the fracture permeability is four orders of magnitude greater than that of the matrix, flow converges into the fractures, accelerates along their length, and re-emerges into the matrix, creating localized acceleration of the brine through the highly permeable pathways of the conductive fractures. The streamline density in the surrounding matrix is noticeably reduced, indicating that transport is dominated by flow through the conductive fractures.

The impact of fracture configuration on the evolution of CO_2 mass fraction is illustrated in Fig. 8. In the base case without fractures, gravitational instabilities develop near the top boundary due to the density difference between CO_2-rich and CO_2-poor brine. These instabilities give rise to downward-propagating convective fingers, which enhance dissolution trapping by increasing the contact area between CO_2 and resident brine (Voskov and Tchelepi, 2012). In the low-permeability fracture case, some vertical finger development cannot cross the barriers, but the overall convective pattern remains similar to the base case. In the high-permeability case, CO_2-rich fluid rapidly enters the conductive fractures, descends to greater depths, and re-enters the matrix, driving large-scale flow patterns on both sides of the fracture network.

Fig. 9 further shows the temporal evolution of both dissolved and residual trapping fractions. Dissolution increases progressively as the CO_2 plume interacts with undersaturated brine. Residual trapping, on the other hand, is primarily controlled by capillary hysteresis. After injection stops, brine, as the wetting phase in most sedimentary formations, imbibes into the trailing edge of the non-wetting CO_2 plume. This imbibition process leaves disconnected and immobile CO_2 ganglia behind (Juanes et al., 2006). In the conductive fracture case, the rapid migration of CO_2 along connected pathways reduces its contact time with the surrounding matrix, limiting capillary trapping and resulting in lower residual immobilization. In contrast, dissolution trapping is higher because the fracture-controlled flow locally enhances mixing and interfacial contact between CO_2-rich and CO_2-poor brine.

4.2. Test case 2: Validation of pEDFM-ADM

Building on Test Case 1, we further evaluate the capability of the proposed pEDFM-ADM framework in capturing the dynamics of CO_2 migration and trapping in Test Case 2 by comparing with a fine-scale solution. The pEDFM-ADM simulations employ two coarse levels, each with a uniform coarsening ratio of 5 in both x- and z- directions. To evaluate the sensitivity of the adaptive resolution control, we test three threshold values for the front-tracking criterion based on local variations in the overall CO_2 mass fraction, $\Delta z_{CO_2} \in \{10^{-1}, 10^{-2}, 10^{-3}\}$. This criterion governs both refinement and coarsening during the simulation, ensuring that high resolution is applied selectively in regions with sharp CO_2 gradients. Over the full simulation cycle, including both injection and post-injection periods, the model captures key processes such as plume propagation, convective mixing, and dissolution, while dynamically adjusting grid resolution in response to the evolving front.

Figs. 10 and 11 present snapshots at $t = 20000$ days for two contrasting fracture scenarios: one with two low-permeability fractures acting as flow barriers ($k_f/k_m = 10^{-6}$), and another with two conductive fractures ($k_f/k_m = 10^4$). For the barrier case, the pEDFM-ADM simulations closely reproduce both the extent and the fine-scale morphology of the plume, including fingering structures. As the refinement threshold tightens, the error drops from 0.43% to 0.14%, accompanied by an increase in the fraction of active grid cells (AGC) from 39% to 91%. Here, active grid cells refer to the fine-scale cells that are explicitly resolved in the simulation at a given time step and higher AGC values mean finer resolution but also greater computational cost. In the conductive-fracture case, even the coarsest setting ($\Delta z_{CO_2} = 10^{-1}$) adequately captures the large-scale convection pattern with only 0.35% error, using merely 37% of the fine-grid resolution.

Fig. 12 complements these visual comparisons by reporting quantitative accuracy and efficiency metrics. Fig. 12(a) and (b) show the differences in pressure and overall mass fraction between pEDFM-ADM and the fine-scale reference solution. Both quantities remain consistently small across the simulation, demonstrating that pEDFM-ADM preserves the accuracy of the fine-scale model. The AGC curves in Fig. 12(c) highlight how the dynamic algorithm selectively refines only the active regions. For the most stringent threshold, the algorithm retains approximately 80% of the fine grid cells on average over the simulation period. As the ADM threshold increases, the number of active cells decreases, which reduces computational cost, but the error in each primary variable correspondingly increases. In this particular test case, the solutions for thresholds of 10^{-2} and 10^{-3} are nearly indistinguishable. These results demonstrate that pEDFM-ADM enables a tunable balance between computational efficiency and accuracy. In both the flow-barrier and conductive-fracture cases, the framework preserves essential features such as solute fingering, and convective mixing, while maintaining acceptable accuracy with reduced computational cost.

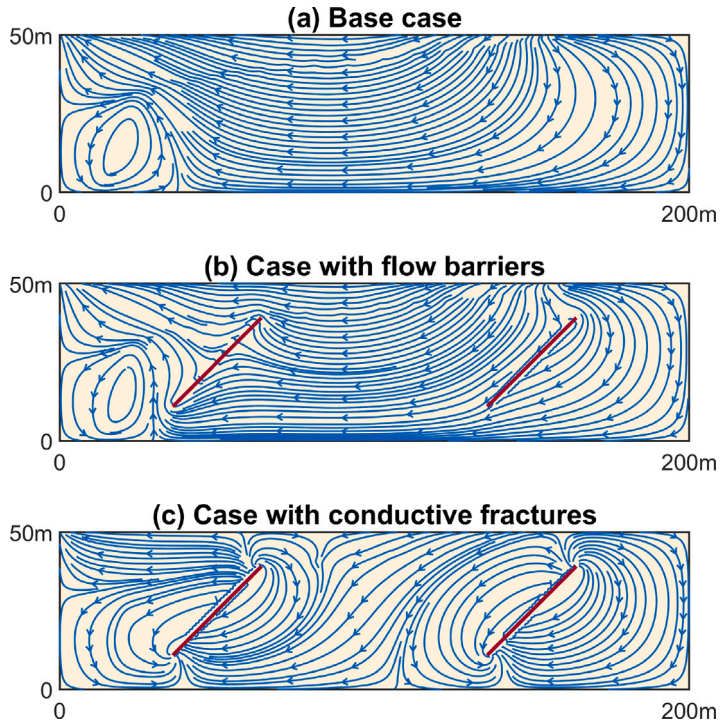

Fig. 7. Streamline distribution of aqueous phase at 1200 days for Test Case 1.

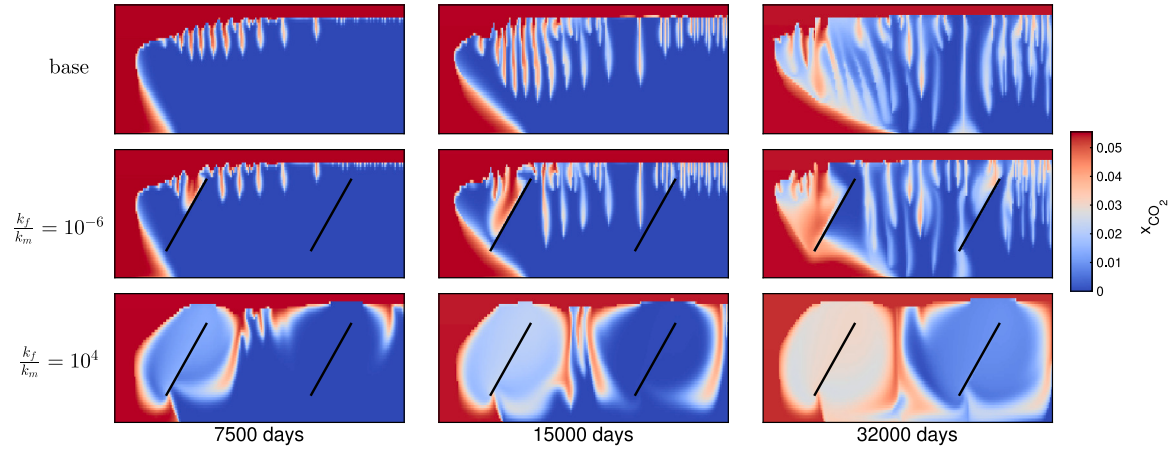

Fig. 8. Snapshots of CO_2 mass fraction at 7500, 15 000, 32 000 days for Test Case 1. The aspect ratio of the figures has been adjusted for improved visualization.

4.3. Test case 3: Fractures with complex geometries

To further demonstrate the effectiveness and generality of the proposed pEDFM-ADM framework, we consider a more challenging scenario involving a complex, irregular fracture network, as illustrated in Fig. 13. The computational domain spans 200 m in the horizontal direction and 50 m vertically, and contains 30 fractures with diverse orientations, lengths, and spatial distributions, including both intersecting and isolated segments, as reported in Wang et al. (2022b).

As with the previous test cases, we simulate two representative scenarios with extreme fracture-matrix permeability contrasts: a low-permeability fracture network with $\log(k_f/k_m) = -6$, and a highly conductive network with $\log(k_f/k_m) = 4$. For each case, pEDFM-ADM simulations are again performed using three different adaptivity thresholds based on Δz_{CO_2}: $\{10^{-1}, 10^{-2}, 10^{-3}\}$. Boundary conditions and fluid properties are consistent with those listed in Table 1.

Figs. 14 and 15 present CO_2 mass fraction distributions at intermediate (2500 days) and late (32 000 days) times, comparing fine-scale reference solutions with pEDFM-ADM results across varying adaptivity thresholds. For the low-permeability fracture network ($\log(k_f/k_m) = -6$), the fractures act as flow barriers that partition the domain and inhibit vertical plume propagation. At 2500 days, the pEDFM-ADM simulations accurately capture both the leading front and finger morphology with high fidelity compared to the fine-scale solution, with an error of $\epsilon = 0.03\%$ at $\Delta z_{CO_2} = 10^{-1}$, while activating only 48% of the grid cells. At 32 000 days, the plume remains largely confined by low-permeability segments, and the pEDFM-ADM results remain consistent with the reference solution, with $\epsilon = 0.32\%$ and 47% active cells at the coarsest threshold.

The high-permeability fracture network ($\log(k_f/k_m) = 4$) functions as a conduit system that channels CO_2 along fracture planes and induces large-scale convective mixing patterns within the matrix. At 2500 days, these transport features are reproduced with $\epsilon = 0.18\%$ using only 37% of the fine grid at $\Delta z_{CO_2} = 10^{-1}$. At 32 000 days, the plume geometry becomes increasingly influenced by fracture-controlled mixing. Resolving these structures requires finer adaptivity: the error

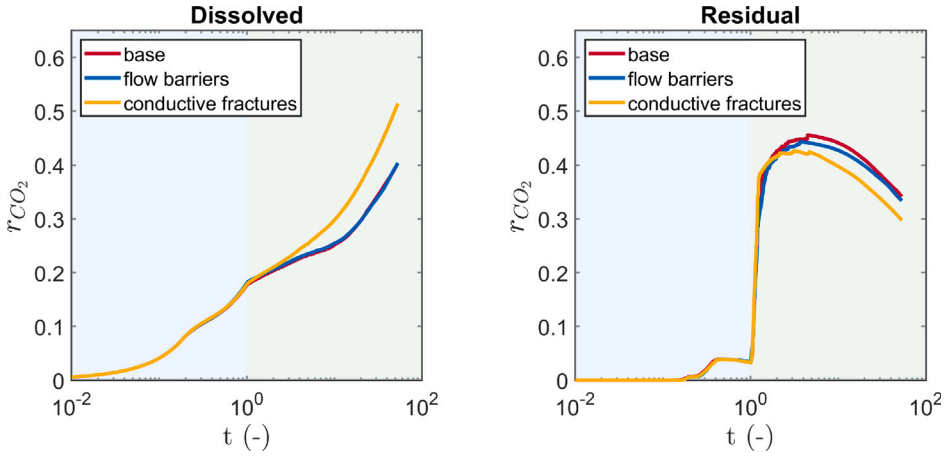

Fig. 9. Temporal evolution of the fraction of injected CO_2 trapped by different mechanisms. The elapsed time (t) is nondimensionalized with respect to the duration of the injection period. The light-blue shaded region denotes the injection phase, while the light-green shaded region corresponds to the post-injection phase.

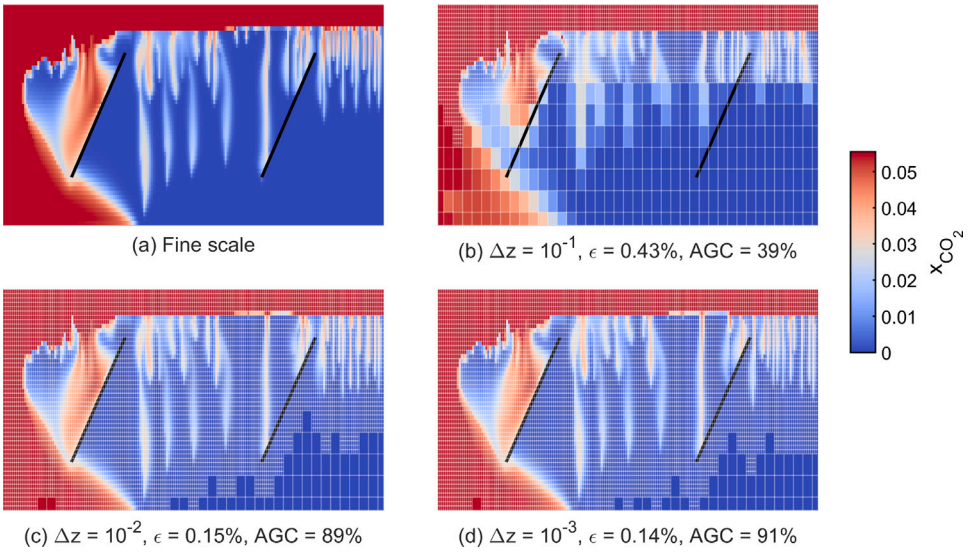

Fig. 10. CO_2 mass fraction profiles after 20 000 days for the case with $\log(k_f/k_m) = -6$, showing the fine and coarse grid levels.

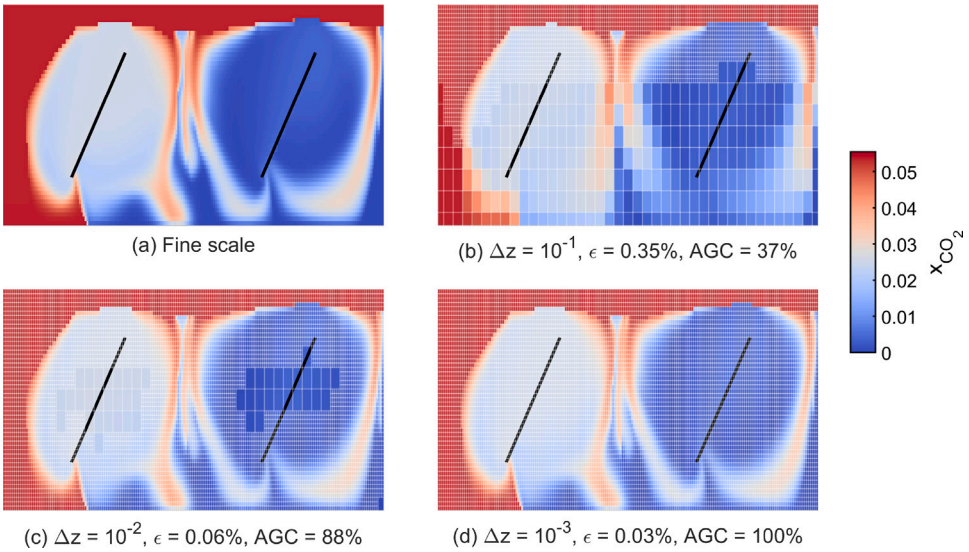

Fig. 11. CO_2 mass fraction profiles after 20 000 days for the case with $\log(k_f/k_m) = 4$, illustrating detailed plume behavior across fine and coarse grid levels.

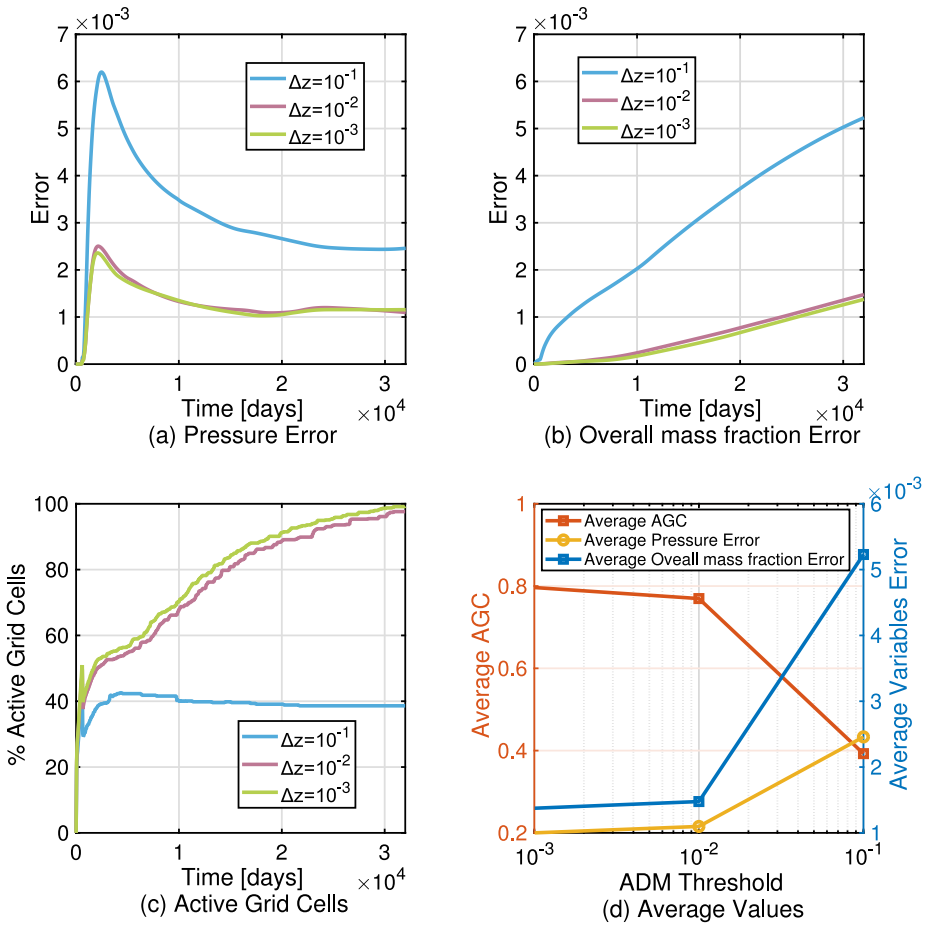

Fig. 12. Error analysis for case with flow barriers, detailing pEDFM-ADM performance across various thresholds, with metrics for pressure, mass fraction errors, and active grid cell usage.

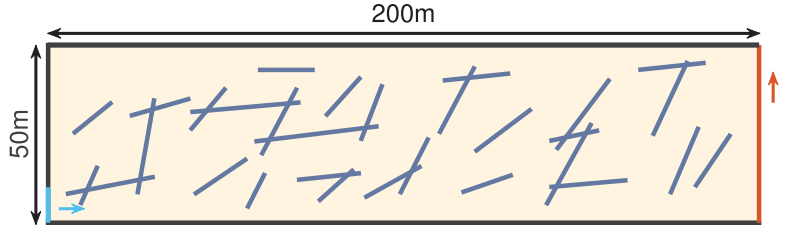

Fig. 13. Schematic of computational domain and fracture geometries for Test Case 3.

decreases from $\epsilon = 0.61\%$ at $\Delta z_{CO_2} = 10^{-1}$ to 0.19% at tighter threshold, with corresponding active cell fraction increasing from 30% to 82%. These comparisons illustrate that the pEDFM-ADM concentrates resolution near the front, and that higher fracture conductivity requires finer spatial resolution to accurately represent plume dynamics.

Fig. 16 quantifies the temporal evolution of errors and the fraction of active grid cells used in the simulation. For the low-permeability fracture network, plume migration is limited by the barrier effect, producing a compact CO_2 plume with relatively sharp z_{CO_2} gradients along its boundary. Since the pEDFM-ADM algorithm refines only in regions of steep gradients, most of the reservoir can be represented on a coarse grid, with fine-scale resolution concentrated along the advancing front. In contrast, for the high-permeability fracture network, the plume rapidly disperses throughout the reservoir, generating large-scale mixing and numerous localized regions of CO_2 gradients. Accurately resolving this transport pattern requires fine-scale resolution across much of the domain, keeping the active cell fraction high for an extended period. Fig. 17 aggregates the dissolved and residual trapping fractions to visualize the total trapping occurring in each simulation. The conductive network exhibits much stronger dissolution due to fracture-induced mixing and enhanced interface area. Residual trapping primarily occurs during the post-injection period. Across all thresholds, including $\Delta z_{CO_2} = 10^{-1}$, the pEDFM-ADM solutions closely follow the fine-scale curves, demonstrating the framework's capability for rapid yet reliable quantification of trapping metrics, even under relatively coarse adaptive thresholds.

4.4. Test case 4: Heterogeneous aquifer with mixed-conductivity fractures

In this section, we consider a complex scenario that couples heterogeneous matrix permeability with fractures of contrasting hydraulic roles (i.e. both conductive fractures and flow barriers). The matrix permeability field is derived from cropped subregion of the SPE10 benchmark dataset ("SPE10Bottom"), characterized by strong spatial correlations and channelized high-permeability streaks (Christie and Blunt, 2001). The same fracture network from Test Case 3 (composed

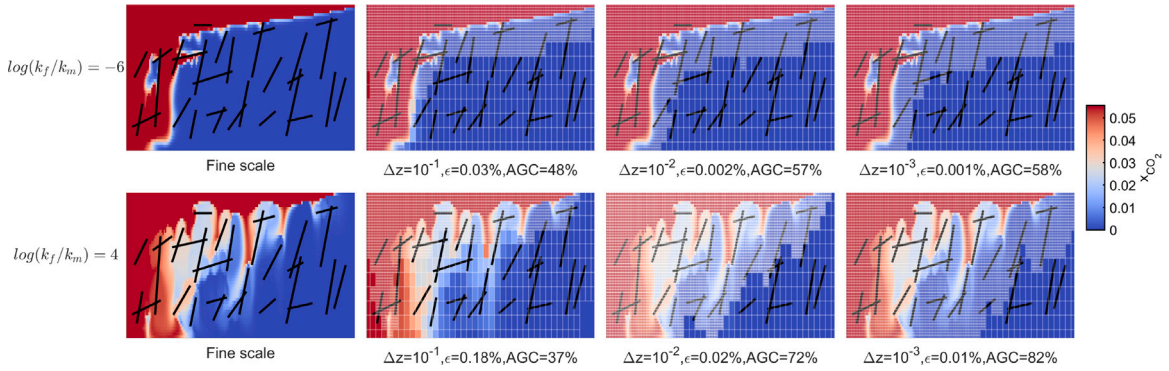

Fig. 14. CO_2 mass fraction profiles at 2500 days for Test Case 3. Fine-scale results are compared with pEDFM-ADM solutions at thresholds 10^{-1}, 10^{-2}, 10^{-3}. Overlaid grid lines show local coarsening levels.

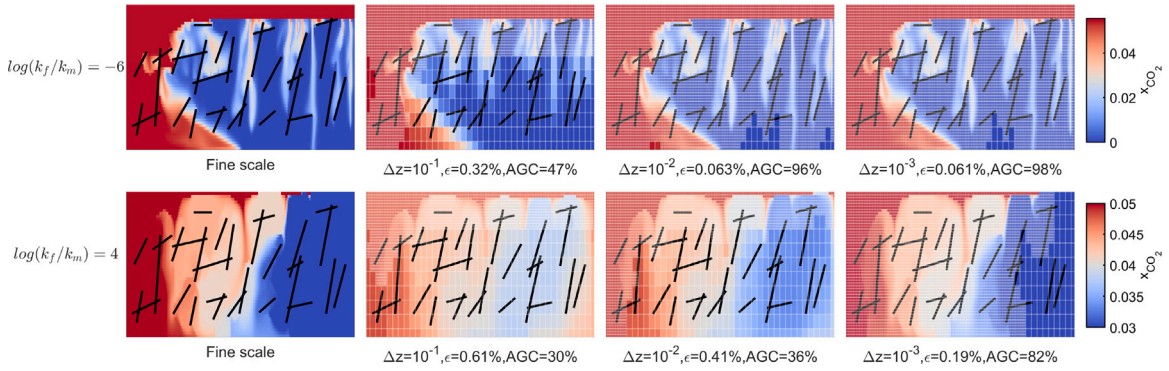

Fig. 15. CO_2 mass fraction profiles at 32 000 days for Test Case 3. Fine-scale results are compared with pEDFM-ADM solutions at thresholds 10^{-1}, 10^{-2}, 10^{-3}. Overlaid grid lines show local coarsening levels.

of 30 fractures) is superimposed on this field. As shown in Fig. 18, white lines denote highly conductive fractures with $k_f = 8.0 \times 10^{-10}$ m^2, while black lines represent low-permeability barriers with $k_f = 8.0 \times 10^{-20}$ m^2. This setup reflects a more geologically realistic subsurface environment where both matrix and fracture heterogeneity influence flow behavior.

Figs. 19 and 20 show CO_2 mass fraction fields at early time (600 days) and late time (20 000 days), respectively, comparing fine-scale reference solutions with pEDFM-ADM results under different refinement thresholds. At 600 days, the plume evolution is primarily governed by the heterogeneous matrix permeability field, with migration strongly aligned along high-permeability pathways and hindered by low-permeability zones. Conductive fractures serve to locally enhance transport where they intersect permeable matrix channels, whereas barrier-type fractures alter flow paths and create compartmentalization. The adaptive pEDFM-ADM approach successfully reproduces these early-stage features: even at the coarsest setting ($\Delta z_{CO_2} = 10^{-1}$), the error remains as low as $\epsilon = 0.10\%$ while activating only 46% of fine grid cells.

By 20 000 days, the CO_2 plume exhibits a substantially more complex structure, shaped by long-range interactions between the underlying matrix heterogeneity and fracture connectivity. The presence of conductive fractures facilitates deep plume penetration and sustains extensive fracture-controlled mixing. At the coarsest refinement level ($\Delta z_{CO_2} = 10^{-1}$), pEDFM-ADM captures large-scale plume distribution but fails to resolve finer structural details, with a error of 0.40% and only 26% of the fine grid cells active. Tighter thresholds ($\Delta z_{CO_2} = 10^{-2}$ and 10^{-3}) recover progressively more fine-scale features, with errors of 0.10% and 0.02% and activate 81% and 99% of the grid, respectively. While this demonstrates the framework's ability to focus resolution in physically significant regions such as fracture intersections and sharp fronts, the trade-off between accuracy and efficiency becomes apparent: the $\Delta z_{CO_2} = 10^{-3}$ case achieves near fine-scale accuracy but offers minimal computational savings due to the high active grid cell count.

As seen in Fig. 21, both pressure and CO_2 mass fraction errors are reported alongside the temporal evolution of the active grid cell fraction, providing a quantitative assessment of solution accuracy and grid activation for this test case. Errors consistently decrease with tighter refinement thresholds, while temporal variations reflect gradual accumulation as the plume interacts with increasingly complex regions of the domain. The averaged metrics in Fig. 21(d) further confirm the accuracy-efficiency trade-off: loose thresholds greatly reduce active fine cell usage but lose fine-scale detail, whereas the tightest threshold achieves near fine-scale accuracy with minimal computational savings because the active grid fraction remains close to 100% for most of the simulation.

Finally, Fig. 22 illustrates the temporal evolution of CO_2 storage mechanisms, including dissolved and residual trapping fractions. Across all thresholds, including the coarsest setting, the pEDFM-ADM framework accurately reproduces the evolution of global storage metrics and maintains close agreement with the fine-scale reference. These results confirm the method's robustness and predictive capability for simulating multiphase, multicomponent flow in complex geological domains containing both matrix heterogeneity and mixed fracture types, reinforcing its potential for practical applications in geological CO_2 sequestration.

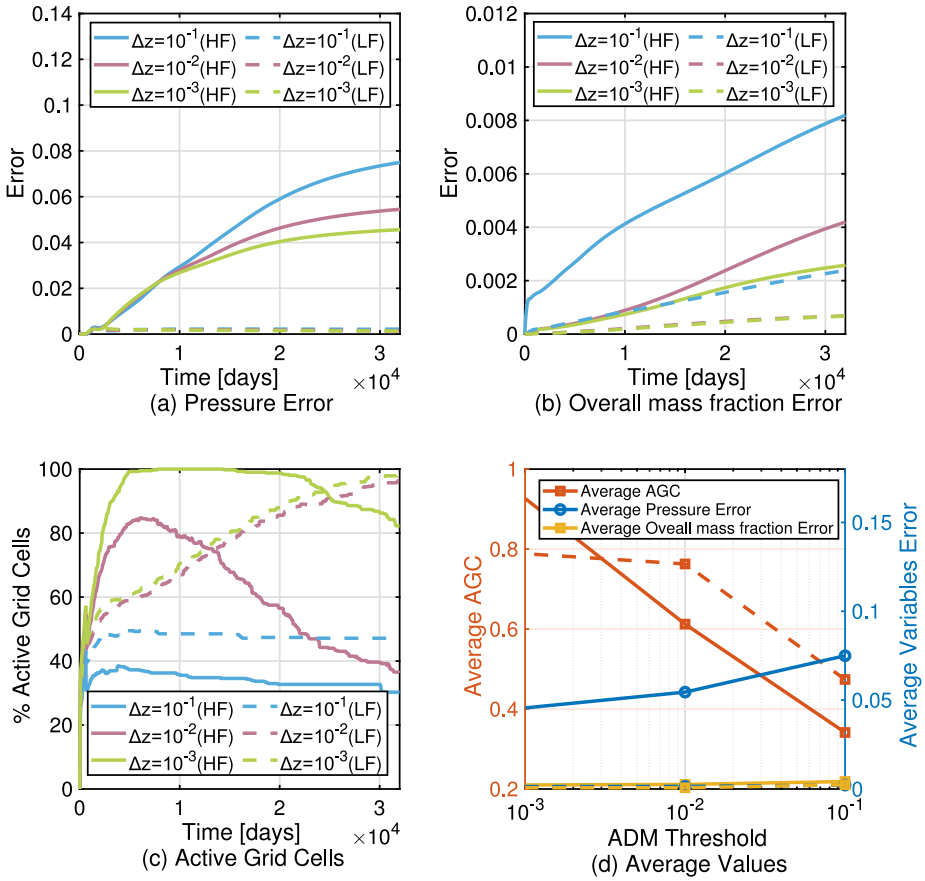

Fig. 16. Quantitative error analysis of pEDFM-ADM solutions for Test Case 3. Pressure and overall CO_2 mass fraction errors are shown alongside the percentage of active grid cells for each coarsening threshold. (HF: high-permeability fractures; LF: low-permeability fractures).

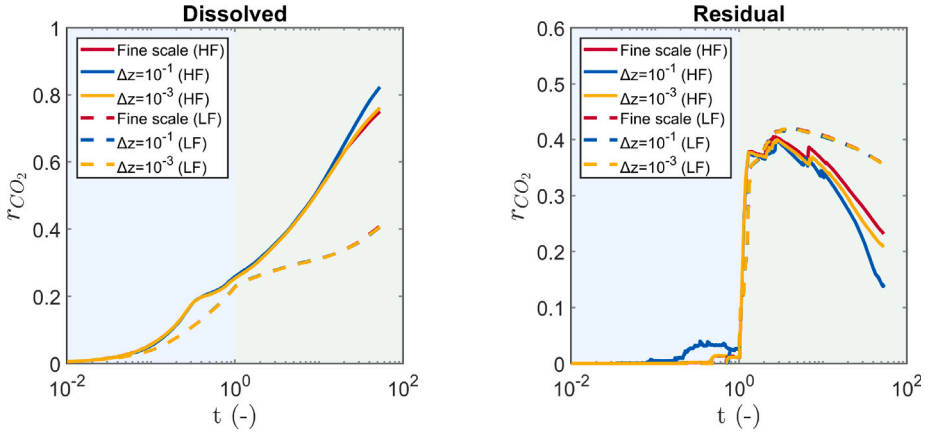

Fig. 17. Temporal evolution of CO_2 trapping mechanisms in Test Case 3. Results are expressed as fractions of the injected CO_2 retained in immobile and dissolved states over dimensionless time. The light-blue shaded region denotes the injection phase, while the light-green shaded region corresponds to the post-injection phase.

5. Conclusions

This study presented a multiscale simulation framework, Projection-based Embedded Discrete Fracture Modeling with Algebraic Dynamic Multilevel method (pEDFM-ADM), for efficient and accurate modeling of CO_2 storage in fractured deep saline aquifers. The framework combines an embedded representation of discrete fractures with an algebraic, front-tracking-based dynamic mesh adaptation strategy, allowing for both grid refinement and coarsening in response to evolving plume fronts during CO_2 migration and trapping.

The method constructs a hierarchy of multilevel grids and localized multiscale basis functions for both matrix and fracture cells. These basis functions are extended to incorporate fracture effects, ensuring accurate matrix–fracture coupling through algebraic prolongation and

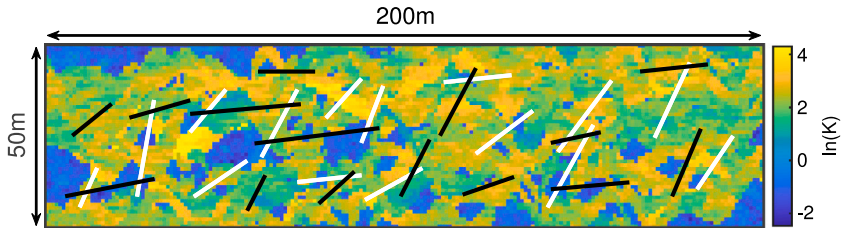

Fig. 18. Log-permeability field $\ln(K)$ of the matrix and fracture configuration for Test Case 4. White segments represent highly conductive fractures, while black segments denote low-permeability barriers.

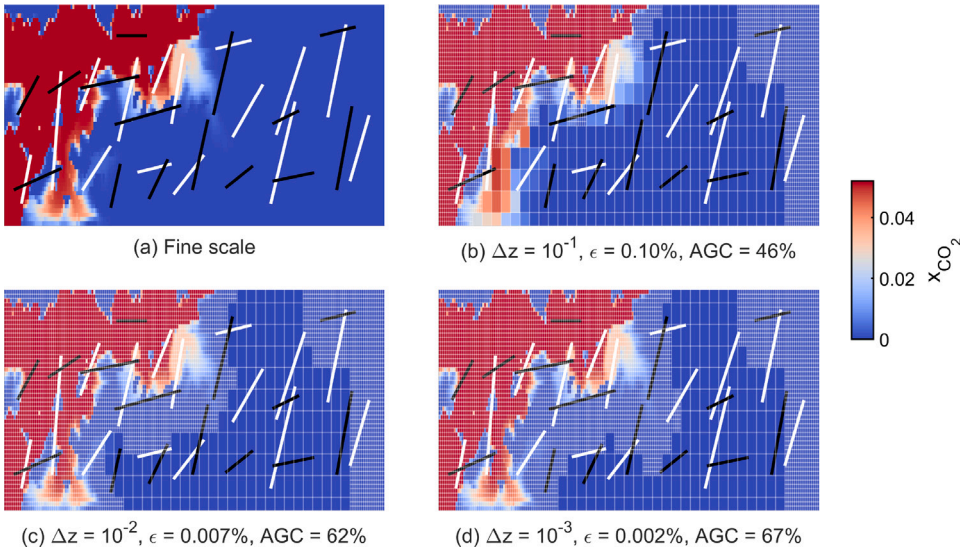

Fig. 19. CO_2 mass fraction profiles after 600 days for Test Case 4. For the pEDFM-ADM simulations, the dynamically refined grid is overlaid as white lines.

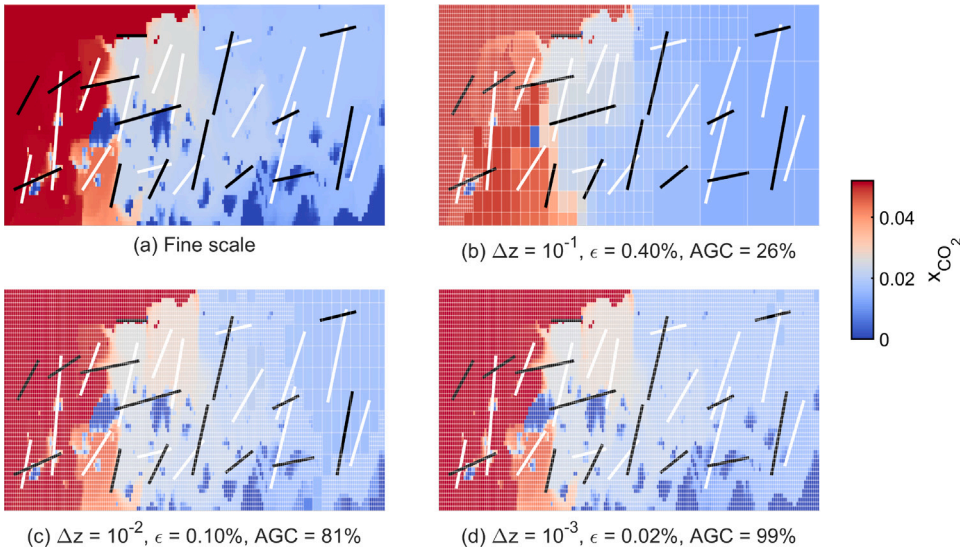

Fig. 20. CO_2 mass fraction profiles after 20 000 days for Test Case 4. For the pEDFM-ADM simulations, the dynamically refined grid is overlaid as white lines.

restriction operators, which enable efficient projection between grid levels.

Through a series of progressively complex test cases, the proposed approach demonstrated its capability to capture multiphase, multicomponent flow phenomena features, including fracture-controlled transport, barrier-induced compartmentalization, dissolution-driven convection, and residual trapping. In scenarios dominated by low-permeability fractures, the method resolved the redirection of flow around low permeability fractures and localized density-driven fingering. In contrast, for highly conductive fractures, the model captured preferential transport and large-scale convective mixing. In all cases, the adaptive mesh strategy ensures that computational resolution is concentrated in physically significant regions, such as plume fronts and fracture intersections, while preserving coarser resolution elsewhere to reduce

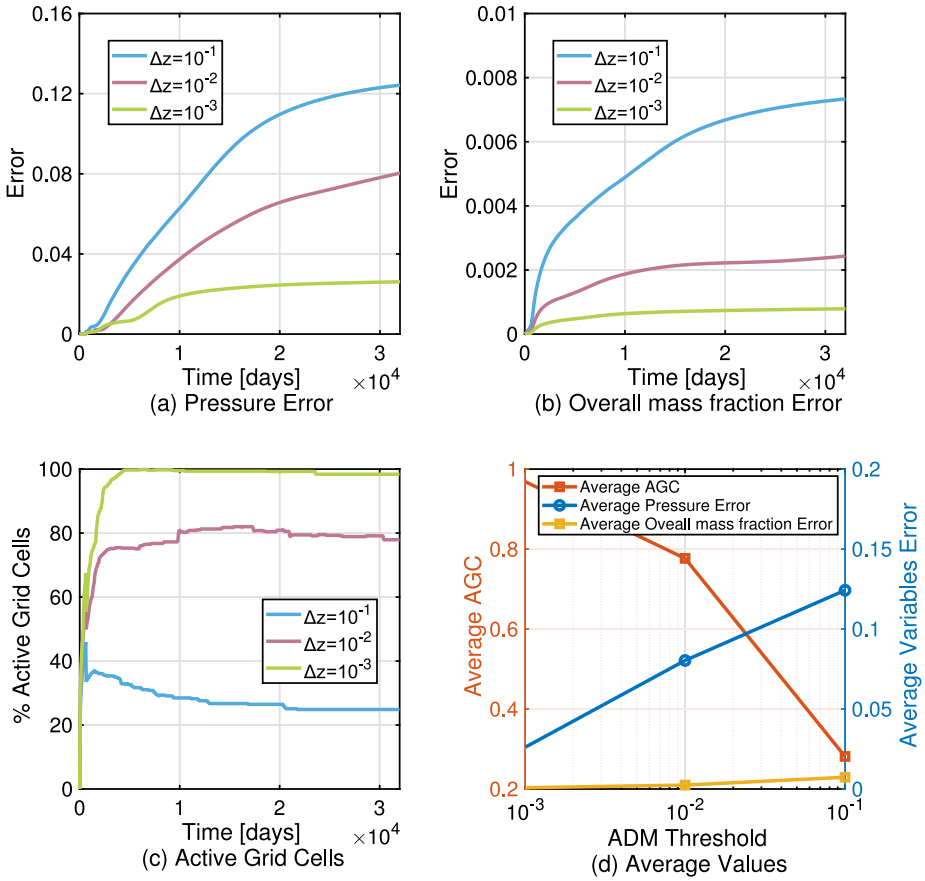

Fig. 21. Error analysis of pEDFM-ADM solutions for Test Case 4. Pressure and overall CO_2 mass fraction errors are shown alongside the percentage of active grid cells for each coarsening threshold.

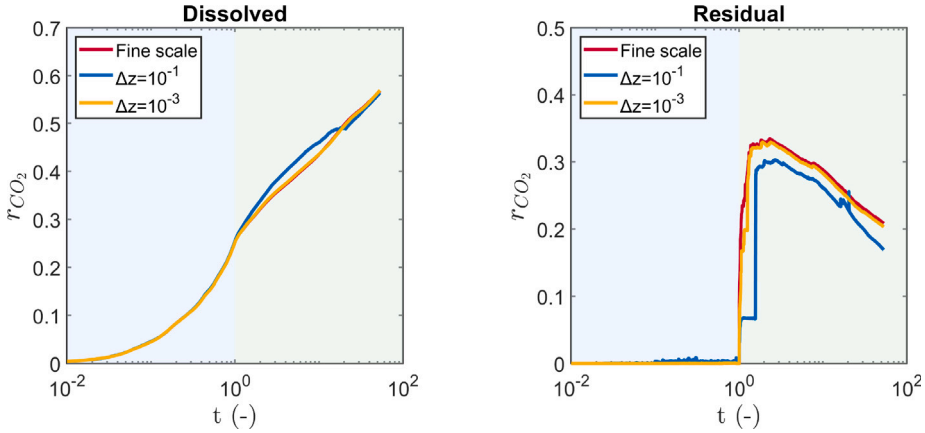

Fig. 22. Temporal evolution of CO_2 trapping mechanisms in Test Case 4. Results are expressed as fractions of the injected CO_2 retained in immobile and dissolved states over dimensionless time. The light-blue shaded region denotes the injection phase, while the light-green shaded region corresponds to the post-injection phase.

computational cost, thereby providing a trade-off between simulation accuracy and computational efficiency.

Importantly, the method preserves key storage metrics across all thresholds, including dissolved and residual CO_2 fractions, thereby confirming its reliability in capturing long-term trapping behavior. These results highlight the potential of projection-based multiscale embedded fracture models as a scalable and predictive tool for assessing CO_2 migration and storage performance in geologically realistic formations.

CRediT authorship contribution statement

Mengjie Zhao: Writing – original draft, Visualization, Validation, Software, Methodology, Conceptualization. **Ryan Haagenson:** Writing – review & editing, Visualization, Methodology, Conceptualization. **Marc Gerritsma:** Writing – review & editing, Supervision, Methodology, Conceptualization. **Hadi Hajibeygi:** Writing – review & editing,

Supervision, Software, Methodology, Funding acquisition, Conceptualization.

Declaration of competing interest

The authors declare that they have no known competing financial interests or personal relationships that could have appeared to influence the work reported in this paper.

Acknowledgments

MZ acknowledges the China Scholarship Council for supporting her PhD work at TU Delft. HH was partly funded by the Dutch Research Council (NWO) under the Talent Scheme Vidi, project ADMIRE. Financial support of the Energi Simulation Chair in Subsurface Storage and Multiscale Modeling is acknowledged. The implementation of this work is made available to the public via the open-source Delft Advanced Reservoir Simulator (DARSim): https://gitlab.com/darsim.

Data availability

Data will be made available on request.

References

Abou-Kassem, J.H., Farouq-Ali, S.M., Islam, M.R., 2013. Petroleum Reservoir Simulations. Elsevier.
Alcalde, J., Flude, S., Wilkinson, M., Johnson, G., Edlmann, K., Bond, C.E., Scott, V., Gilfillan, S.M., Ogaya, X., Haszeldine, R.S., 2018. Estimating geological CO_2 storage security to deliver on climate mitigation. Nat. Commun. 9 (1), 2201.
Bachu, S., 2008. CO_2 storage in geological media: Role, means, status and barriers to deployment. Prog. Energy Combust. Sci. 34 (2), 254–273.
Bashir, A., Ali, M., Patil, S., Aljawad, M.S., Mahmoud, M., Al-Shehri, D., Hoteit, H., Kamal, M.S., 2024. Comprehensive review of CO_2 geological storage: Exploring principles, mechanisms, and prospects. Earth-Sci. Rev. 249, 104672.
Benson, S.M., Cole, D.R., 2008. CO_2 sequestration in deep sedimentary formations. Elements 4 (5), 325–331.
Berkowitz, B., 2002. Characterizing flow and transport in fractured geological media: A review. Adv. Water Resour. 25 (8–12), 861–884.
Berre, I., Doster, F., Keilegavlen, E., 2019. Flow in fractured porous media: A review of conceptual models and discretization approaches. Transp. Porous Media 130 (1), 215–236.
Boot-Handford, M.E., Abanades, J.C., Anthony, E.J., Blunt, M.J., Brandani, S., Mac Dowell, N., Fernández, J.R., Ferrari, M.-C., Gross, R., Hallett, J.P., et al., 2014. Carbon capture and storage update. Energy & Environ. Sci. 7 (1), 130–189.
Bui, M., Adjiman, C.S., Bardow, A., Anthony, E.J., Boston, A., Brown, S., Fennell, P.S., Fuss, S., Galindo, A., Hackett, L.A., et al., 2018. Carbon capture and storage (CCS): The way forward. Energy & Environ. Sci. 11 (5), 1062–1176.
Cavalcante, T.d.M., Souza, A.C., Hajibeygi, H., Carvalho, D.K., Lyra, P.R., 2024. Simulation of two-phase flow in 3D fractured reservoirs using a projection-based embedded discrete fracture model on unstructured tetrahedral grids (pEDFM-U). Adv. Water Resour. 187, 104679.
Christie, M.A., Blunt, M.J., 2001. Tenth SPE comparative solution project: A comparison of upscaling techniques. SPE Reserv. Eval. Eng. 4 (04), 308–317.
Cusini, M., Fryer, B., van Kruijsdijk, C., Hajibeygi, H., 2018. Algebraic dynamic multilevel method for compositional flow in heterogeneous porous media. J. Comput. Phys. 354, 593–612.
Cusini, M., van Kruijsdijk, C., Hajibeygi, H., 2016. Algebraic dynamic multilevel (ADM) method for fully implicit simulations of multiphase flow in porous media. J. Comput. Phys. 314, 60–79.
Efendiev, Y., Lee, S., Li, G., Yao, J., Zhang, N., 2015. Hierarchical multiscale modeling for flows in fractured media using generalized multiscale finite element method. GEM Int. J. Geomath. 6, 141–162.
Fanchi, J.R., 2005. Principles of Applied Reservoir Simulation. Elsevier.
Hajibeygi, H., Bonfigli, G., Hesse, M.A., Jenny, P., 2008. Iterative multiscale finite-volume method. J. Comput. Phys. 227 (19), 8604–8621.
Hajibeygi, H., Karvounis, D., Jenny, P., 2011. A hierarchical fracture model for the iterative multiscale finite volume method. J. Comput. Phys. 230 (24), 8729–8743.
HosseiniMehr, M., Cusini, M., Vuik, C., Hajibeygi, H., 2018. Algebraic dynamic multilevel method for embedded discrete fracture model (F-ADM). J. Comput. Phys. 373, 324–345.
HosseiniMehr, M., Piguave Tomala, J., Vuik, C., Al Kobaisi, M., Hajibeygi, H., 2022. Projection-based embedded discrete fracture model (pEDFM) for flow and heat transfer in real-field geological formations with hexahedral corner-point grids. Adv. Water Resour. 159, 104091.
HosseiniMehr, M., Vuik, C., Hajibeygi, H., 2020. Adaptive dynamic multilevel simulation of fractured geothermal reservoirs. J. Comput. Phys.: X 7, 100061.
Hoteit, H., Firoozabadi, A., 2008. Numerical modeling of two-phase flow in heterogeneous permeable media with different capillarity pressures. Adv. Water Resour. 31 (1), 56–73.
Hou, T.Y., Wu, X.-H., 1997. A multiscale finite element method for elliptic problems in composite materials and porous media. J. Comput. Phys. 134 (1), 169–189.
Jenny, P., Lee, S., Tchelepi, H.A., 2003. Multi-scale finite-volume method for elliptic problems in subsurface flow simulation. J. Comput. Phys. 187 (1), 47–67.
Juanes, R., Spiteri, E., Orr Jr., F., Blunt, M., 2006. Impact of relative permeability hysteresis on geological CO_2 storage. Water Resour. Res. 42 (12).
Karimi-Fard, M., Durlofsky, L.J., Aziz, K., 2004. An efficient discrete-fracture model applicable for general-purpose reservoir simulators. SPE J. 9 (02), 227–236.
Krevor, S., De Coninck, H., Gasda, S.E., Ghaleigh, N.S., de Gooyert, V., Hajibeygi, H., Juanes, R., Neufeld, J., Roberts, J.J., Swennenhuis, F., 2023. Subsurface carbon dioxide and hydrogen storage for a sustainable energy future. Nat. Rev. Earth & Environ. (ISSN: 2662-138X) 4 (2), 102–118.
Lee, S.H., Lough, M., Jensen, C., 2001. Hierarchical modeling of flow in naturally fractured formations with multiple length scales. Water Resour. Res. 37 (3), 443–455.
Lee, S., Wolfsteiner, C., Tchelepi, H., 2008. Multiscale finite-volume formulation for multiphase flow in porous media: Black oil formulation of compressible, three-phase flow with gravity. Comput. Geosci. 12, 351–366.
Li, L., Lee, S.H., 2008. Efficient field-scale simulation of black oil in a naturally fractured reservoir through discrete fracture networks and homogenized media. SPE Reserv. Eval. Eng. 11 (04), 750–758.
Matthäi, S.K., Mezentsev, A., Belayneh, M., 2007. Finite element–node-centered finite-volume two-phase-flow experiments with fractured rock represented by unstructured hybrid-element meshes. SPE Reserv. Eval. Eng. 10 (06), 740–756.
Metz, B., Davidson, O., De Coninck, H., Loos, M., Meyer, L., 2005. IPCC Special Report on Carbon Dioxide Capture and Storage. Cambridge University Press, Cambridge.
Michelsen, M.L., Mollerup, J.M., 2004. Thermodynamic Models: Fundamentals & Computational Aspects. Tie-Line Publications Holte, Denmark.
Moinfar, A., Varavei, A., Sepehrnoori, K., Johns, R.T., 2013. Development of a coupled dual continuum and discrete fracture model for the simulation of unconventional reservoirs. In: SPE Reservoir Simulation Conference. SPE, p. SPE–163647.
Moinfar, A., Varavei, A., Sepehrnoori, K., Johns, R.T., 2014. Development of an efficient embedded discrete fracture model for 3D compositional reservoir simulation in fractured reservoirs. SPE J. 19 (02), 289–303.
Oak, M.J., Baker, L.E., Thomas, D., 1990. Three-phase relative permeability of berea sandstone. J. Pet. Technol. 42 (08), 1054–1061.
Praditia, T., Helmig, R., Hajibeygi, H., 2018. Multiscale formulation for coupled flow-heat equations arising from single-phase flow in fractured geothermal reservoirs. Comput. Geosci. 22, 1305–1322.
Prausnitz, J.M., Lichtenthaler, R.N., De Azevedo, E.G., 1998. Molecular Thermodynamics of Fluid-Phase Equilibria. Pearson Education.
Rao, X., He, X., Du, K., Kwak, H., Yousef, A., Hoteit, H., 2024. A novel projection-based embedded discrete fracture model (pEDFM) for anisotropic two-phase flow simulation using hybrid of two-point flux approximation and mimetic finite difference (TPFA-MFD) methods. J. Comput. Phys. 499, 112736.
Reed, M.H., 1982. Calculation of multicomponent chemical equilibria and reaction processes in systems involving minerals, gases and an aqueous phase. Geochim. Cosmochim. Acta 46 (4), 513–528.
Rutqvist, J., Rinaldi, A.P., Cappa, F., Jeanne, P., Mazzoldi, A., Urpi, L., Guglielmi, Y., Vilarrasa, V., 2016. Fault activation and induced seismicity in geological carbon storage–lessons learned from recent modeling studies. J. Rock Mech. Geotech. Eng. 8 (6), 789–804.
Rutqvist, J., Vasco, D.W., Myer, L., 2010. Coupled reservoir-geomechanical analysis of CO_2 injection and ground deformations at In Salah, Algeria. Int. J. Greenh. Gas Control. 4 (2), 225–230.
Sahimi, M., 2011. Flow and Transport in Porous Media and Fractured Rock: from Classical Methods to Modern Approaches. John Wiley & Sons.
Sokama-Neuyam, Y.A., Boakye, P., Aggrey, W.N., Obeng, N.O., Adu-Boahene, F., Woo, S.H., Ursin, J.R., 2020. Theoretical modeling of the impact of salt precipitation on CO_2 storage potential in fractured saline reservoirs. ACS Omega 5 (24), 14776–14785.
Spycher, N., Pruess, K., Ennis-King, J., 2003. CO_2-H_2O mixtures in the geological sequestration of CO_2. I. assessment and calculation of mutual solubilities from 12 to 100 °C and up to 600 bar. Geochim. Cosmochim. Acta 67 (16), 3015–3031.
Szulczewski, M.L., MacMinn, C.W., Herzog, H.J., Juanes, R., 2012. Lifetime of carbon capture and storage as a climate-change mitigation technology. Proc. Natl. Acad. Sci. 109 (14), 5185–5189.
Ţene, M., Al Kobaisi, M.S., Hajibeygi, H., 2016. Algebraic multiscale method for flow in heterogeneous porous media with embedded discrete fractures (F-AMS). J. Comput. Phys. 321, 819–845.
Ţene, M., Bosma, S.B., Al Kobaisi, M.S., Hajibeygi, H., 2017. Projection-based embedded discrete fracture model (pEDFM). Adv. Water Resour. 105, 205–216.
Van Genuchten, M.T., 1980. A closed-form equation for predicting the hydraulic conductivity of unsaturated soils. Soil Sci. Am. J. 44 (5), 892–898.

Voskov, D.V., Tchelepi, H.A., 2012. Comparison of nonlinear formulations for two-phase multi-component EoS based simulation. J. Pet. Sci. Eng. 82, 101–111.
Wang, Y., Vuik, C., Hajibeygi, H., 2022a. Analysis of hydrodynamic trapping interactions during full-cycle injection and migration of CO_2 in deep saline aquifers. Adv. Water Resour. 159, 104073.
Wang, Y., Vuik, C., Hajibeygi, H., 2022b. CO_2 storage in deep saline aquifers: impacts of fractures on hydrodynamic trapping. Int. J. Greenh. Gas Control 113, 103552.
Zhao, M., Gerritsma, M., Al Kobaisi, M., Hajibeygi, H., 2025. Algebraic dynamic multilevel (ADM) method for CO_2 storage in heterogeneous saline aquifers. J. Comput. Phys. 539, 114202.